J. Fluid Mech. (2020), *vol.* 905, A4.
Published by Cambridge University Press
doi:10.1017/jfm.2020.716

Dissipation element analysis of non-premixed jet flames

D. Denker[1],†, **A. Attili**[1], **J. Boschung**[1], **F. Hennig**[1], **M. Gauding**[2], **M. Bode**[1] **and H. Pitsch**[1]

[1]Institute for Combustion Technology, RWTH Aachen University, Templergraben 64, Aachen 52062, Germany

[2]CORIA – CNRS UMR 6614, Saint Etienne du Rouvray, France

(Received 17 December 2019; revised 10 July 2020; accepted 15 August 2020)

The dissipation element analysis is applied to the mixture fraction fields of a series of datasets from direct numerical simulations of non-premixed temporally evolving jet flames with jet Reynolds numbers ranging from 4500 to 10 000 and varying stoichiometric mixture fractions. Dissipation elements are space-filling regions where a scalar field behaves monotonically and allow for the analysis of scalar fields in homogeneous isotopic turbulence as well as in complex, highly inhomogeneous and anisotropic flows such as turbulent flames. Statistics of the dissipation element parameters of non-premixed flames are compared to those obtained from non-reacting jets. It is found that the universality of the normalized length distribution of the dissipation elements observed in non-reacting cases also holds true for the reacting flows. The characteristic scaling with the Kolmogorov micro-scale η is obtained as well. The effects of combustion on the scalar difference in the dissipation elements are shown and are found to diminish as the Reynolds number and the fuel dilution is increased. The dissipation elements provide the means for a local comparison of the turbulent and characteristic flame scales. A new regime diagram for non-premixed combustion is introduced using coherent structures in the scalar fields, the dissipation element parameters for a local classification of the turbulent flame surface into flamelet-like zones and fine-scale mixing zones in addition to the burning and non-burning zones. The soundness of the regime diagram and the potential consequences for combustion modelling in the individual regimes is demonstrated by the investigation of the correlation between the chemical field and the dissipation element parameters in the individual regimes.

Key words: turbulent reacting flows, isotropic turbulence

1. Introduction

There are several regimes of interest in turbulent combustion. One that is very frequently encountered is the flamelet regime, where chemistry is relatively fast and reactions take place in thin layers. Many technical applications fall into this regime; therefore, prediction methods based on the flamelet concept are often used to model combustion in engines and gas turbines. In this framework, a turbulent flame is viewed as an ensemble of

---

† Email address for correspondence: d.denker@itv.rwth-aachen.de

thin flamelet structures. The flamelet structure is laminar in nature and attached to an instantaneous flame surface, which is corrugated by turbulence. The concept applies to premixed as well as non-premixed combustion. In the case of non-premixed combustion, the assumption of infinitely fast reactions leads to the flame sheet model having an infinitely thin flame structure. As the turbulent mixing is the sole rate-determining process in this regime, the description of non-premixed combustion can be fully described by the transport of the mixture fraction

$$Z = \frac{m_1}{m_1 + m_2} \tag{1.1}$$

with m_1 and m_2 denoting the local mass originating of the fuel and the oxidizer, respectively.

The departure from this limit requires the consideration of finite rate chemistry and can be described by the laminar diffusion flamelet concept (Peters 1984). Flamelet equations can be derived by transforming the transport equations for temperature and species mass fractions into equations with the mixture fraction Z as the independent variable, yielding equations for the species fractions and temperature as

$$\rho\frac{\partial Y_\alpha}{\partial t} - \rho\frac{\chi}{2}\frac{\partial^2 Y_\alpha}{\partial Z^2} = \omega_\alpha, \quad \alpha = 1, 2, \ldots, k, \tag{1.2}$$

$$\rho\frac{\partial T}{\partial t} - \rho\frac{\chi}{2}\frac{\partial^2 T}{\partial Z^2} = \omega_T, \tag{1.3}$$

where χ is the scalar dissipation rate

$$\chi = 2D\left(\frac{\partial Z}{\partial x_i}\right)^2. \tag{1.4}$$

In the equation for the chemical species, ρ is the density, Y_α is the mass fraction of species α, t is the time, Z is the mixture fraction and ω_α is the chemical source term for species α. In the temperature equation, T is the temperature, ω_T is the heat release term due to chemical reactions and D is the diffusion coefficient of the mixture fraction. Since transport in the outer, chemically inert structure of the flame is mostly governed by turbulence, which leads to similar transport for all scalars (Attili *et al.* 2016), all Lewis numbers are assumed be unity $Le_\alpha = \lambda/(c_p\rho D_\alpha) = 1$, with the thermal conductivity λ, the heat capacity c_p and the diffusion coefficient of the species D_α. Additional terms containing spatial derivatives orthogonal to Z, can be neglected to the leading order. The scalar dissipation rate χ serves as the quantity which connects the reacting scalar field to the turbulent flow field.

For intense turbulence, when turbulent scales are small compared to the scales of the flame, the implied separation of turbulent and chemical scales in the laminar diffusion flamelet concept is expected to fail (Bilger *et al.* 2005; Pope 2013). The flame structure and the rate of mixing then start to be affected by interactions between reaction, diffusion and turbulent straining. Another shortcoming is that even in the case of thin structures for the combustion reactions not all reactions are sufficiently fast. This is the case for the chemical processes governing pollutants like NO_x and soot, because their chemistry may be comparably slow. Furthermore, close to extinction or during ignition, when combustion becomes slow or when chemistry competes with diffusive losses in more than one direction, which is known as the edge flame effect (Favier & Vervisch 2001), the flamelet assumption of a thin one-dimensional layer will cease to be valid.

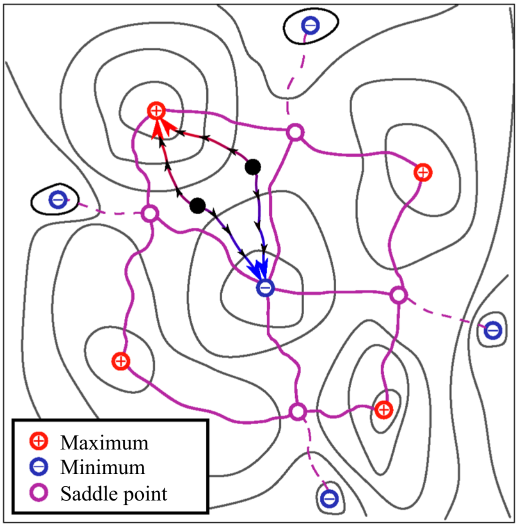

FIGURE 1. Exemplary decomposition of a two-dimensional scalar field by means of a DE analysis. Iso-scalar lines are shown in black. The black symbols show two sample points with associated gradient trajectories towards the scalar maximum (red) and minimum (blue).

To identify and analyse spatial regions of the turbulent reacting flow, which either correspond to flamelet-'friendly' conditions or are dominated by small-scale turbulence and extinction-inducing turbulence intensities, a systematic method for compartmentalization of the turbulent fields is required. A method for a physically motivated decomposition of turbulent scalar fields is the dissipation element (DE) analysis. This analysis considers space-filling spatial regions of a scalar field and has been proposed by Wang & Peters (2006, 2008). DEs are constructed by using gradient trajectories. Starting from every point in the field, a scalar gradient trajectory in the ascending direction will reach a maximum point, and in the descending direction, it will reach a minimum point. A DE is defined as the spatial region from which the same pair of maximum and minimum points is reached by scalar gradient trajectories. Within this region, the scalar field is monotonic making DEs equivalent to Morse–Smale complexes in topology (Schnorr *et al.* 2020). This method of identification of DEs is shown in a schematic fashion in figure 1.

DEs are characterized by two parameters, henceforth called DE parameters: the length ℓ is defined as the linear distance between the minimum and maximum points and $\Delta\phi$ is the difference of the scalar value at these two points. In addition to these two DE parameters, a measure for the scalar gradient can be formed as $g = \Delta\phi/\ell$.

In Wang & Peters (2006, 2008), Gampert *et al.* (2010), Gampert *et al.* (2011), Peters (2012), Gampert *et al.* (2013*a*) and Gampert, Schaefer & Peters (2013*b*), three-dimensional (3-D) direct numerical simulations (DNS) of non-reactive flows were performed in order to obtain the statistics of the DE parameters in turbulent flows. The joint probability density function (jPDF) $P(\ell, \Delta\phi)$ of the two DE parameters $\Delta\phi$ and ℓ is expected to be sufficient to statistically reconstruct most of the scalar field. Several physical effects can be identified in this jPDF, such as the presence of ramp-cliff structures, annihilation of DEs due to molecular diffusion and high spatial gradients caused by intermittency. In these studies, the DE analysis provided a valuable tool for describing and investigating the effect of turbulent and diffusive transport on scalar fields.

Applying DE analysis to reacting turbulent flows provides multiple additional modes of assessment and a new interpretation of DEs in this physical context. It allows the investigation of non-local effects and interactions in complex combustion conditions by providing a well-parametrized and physically meaningful frame of reference. Further, by investigating the interaction between turbulence and combustion chemistry locally within individual DEs, flow dynamics and topology can be considered, while they would otherwise be lost in the averaging procedure used in conventional statistical approaches.

The DE analysis was first applied to the DNS of a non-premixed flame by Gauding *et al.* (2017), where DEs were used to compartmentalize regions of the scalar field which are either connected by diffusive flux to the flame front, the turbulent core region or the outer regions of the flow. Additionally, DE analysis was applied to temperature fields by Denker *et al.* (2019) to investigate the effects of the premixed flame front on turbulent scalar fields in a series of premixed jet flames (Luca *et al.* 2019). The source term present in the temperature fields resulted in a distinct departure from the characteristic features of the DE parameters observed in non-reacting flows.

The DE analysis is applied here to the series of reacting DNS of non-premixed combustion outlined in the next section. In addition, selected non-reactive cases are also considered for comparison. In particular, statistics of the DE parameters are compared among the reacting and non-reacting cases to evaluate the effect of heat release on the scalar fields. The correlation of DE parameters and reacting scalars is investigated to demonstrate the importance of considering non-local effects in the investigated combustion conditions. A comparison of the flame scales with the local turbulent scales provided by the DEs is used to define a new regime diagram for turbulent non-premixed combustion based on the DE parameters. Contrary to conventional approaches to regime classifications, which employ global statistical quantities, the regimes are based on the instantaneous scalar topology and therefore allow for the coexistence and assessment of multiple regimes in a single flame. Finally, the regime diagram is used in a local classification of the combustion of the individual cases.

2. Configurations and numerical methods

2.1. *DNS configuration of the reactive and non-reactive jets*

The configuration selected for this study is a temporally evolving planar jet. This configuration lends itself to the DNS as it provides a good ratio between grid points and the overall volume of reacting flow. Besides displaying self-similarity in non-reacting configurations, the two statistically homogeneous directions simplify the computation of well-converged statistics.

Three different jet Reynolds numbers $Re_{jet} = \bar{U}_0 H_0/\nu_{fuel}$, with initial mean jet bulk velocity $\bar{U}_0$, initial jet width H_0 and kinematic viscosity ν_{fuel} of the fuel, were realized. The values of the Reynolds numbers range from 4500 to 10 000.

Multiple Reynolds numbers are required to investigate the distinctive scaling of DE parameters, which was observed in non-reacting flows by Wang & Peters (2006, 2008, 2013). In addition to the change in Reynolds numbers, two different dilutions of the fuel stream were used for the lowest Reynolds number. These four cases will be referred to as the low *Re* low dilution case, the low *Re* high dilution case, the intermediate *Re* case and the high *Re* case. The turbulent Damköhler number $Da = \chi_q H/U_{c,0}$ is set to $Da = 0.125$ for the low *Re* low dilution case and the low *Re* high dilution case and to $Da = 0.15$ for the other two high dilution cases. These values were chosen to induce local extinction and provide the basis for the investigation of extinction processes. At the final time step of the

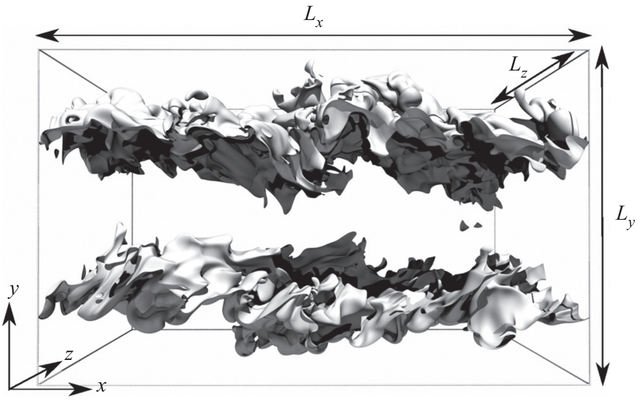

FIGURE 2. General set-up of the DNS investigated in this study. The grey iso-surface indicates the position of the stoichiometric mixture fraction.

simulation, this resulted in approximately 5 %, 11 %, 16 % and 24 % of extinguished flame surface for the *Re* low dilution case, for the *Re* high dilution case, for the intermediate *Re* case, and high *Re* case, respectively.

The oxidizer stream in all reacting cases is air, consisting of oxygen $Y_{O_2,1} = 0.232$ and nitrogen $Y_{N_2,1} = 0.768$. The fuel stream consists of highly diluted methane with $Y_{CH_4,2} = 0.232$ for the low dilution case and $Y_{CH_4,2} = 0.07$ for the high dilution cases. The indices 1 and 2 indicate the oxidizer and the fuel properties, respectively. The dilution of the fuel stream is achieved with N_2. This results in a stoichiometric mixture fraction of $Z_{st} = 0.2$ for the low *Re* low dilution case and $Z_{st} = 0.45$ for the low *Re* high dilution case, the intermediate *Re* case and the high *Re* case. These high dilutions were chosen for two reasons: First, to provide sufficient distance between the turbulent/non-turbulent interface (TNTI) and the flame surface. Second, to provide a wide reaction zone thickness in mixture fraction space δZ_r. The temperature for both oxidizer and fuel was set to $T_1 = T_2 = 500$ K for the low dilution case. To increase the resistance to the turbulence-induced strain, the temperature for the high dilution cases was raised to $T_1 = T_2 = 680$ K. The quenching dissipation rate for all cases is $\chi_q = 120\ \mathrm{s}^{-1}$.

The flow configuration of the reacting cases is shown schematically in figure 2. The domains are periodic in the streamwise x-direction and spanwise z-direction. Boundary conditions in the cross-wise y-direction were chosen as outlets (Ol'shanskii & Staroverov 2000).

This resolution was chosen to ensure a sufficiently resolved reaction zone with a minimum thickness of the OH-layer of 10 grid points at all times. This resolution was used in a number of DNS studies of non-premixed combustion for similar configurations (Hawkes *et al.* 2007; Attili *et al.* 2014), where the quality of the results and the resolution requirements where assessed in detail. The minimum Kolmogorov scale is $\eta = 209\ \mu\mathrm{m}$, with $\eta = \nu^{3/4}\varepsilon^{-1/4}$, for the low *Re* low dilution case, $\eta = 281\ \mu\mathrm{m}$ for the low *Re* high dilution case, $\eta = 245\ \mu\mathrm{m}$ for the intermediate *Re* case and $\eta = 233\ \mu\mathrm{m}$ for the high *Re* case. From this follows that $\Delta/\eta \approx 0.76$, $\Delta/\eta \approx 0.74$, $\Delta/\eta \approx 0.85$ and $\Delta/\eta \approx 0.86$, respectively. This high resolution is required for a meaningful result of a DE analysis (Wang & Peters 2006). Additional details regarding the numerical and physical parameters of the DNS are summarized in table 1.

The velocity field in the jet core was initialized with instantaneous realizations of turbulent channel flows. The mixture fraction field was initialized by integrating

	Low *Re* low dilution case	Low *Re* high dilution case	Intermediate *Re* case	High *Re* case	Non-reacting case I	Non-reacting case II
$\bar{U}_0$ (m s^{-1})	12.1	16.0	16.0	20.7	16.0	1.0
H_0 (mm)	15	18.7	25	32.3	25	1.0
$Re_{jet,0}$	4500	4500	6000	10 000	6000	9850
Da	0.125	0.125	0.15	0.15	—	—
Z_{st}	0.2	0.45	0.45	0.45	—	—
L_x/H_0	8	8.2	8.5	8.5	8.5	6π
L_y/H_0	10	10.2	8.0	8.2	8.0	12.5
L_z/H_0	5.3	5.5	6.4	6.4	6.4	6π
N_x	768	768	1024	1280	1024	2560
N_y	1024	768	768	960	768	1312
N_z	512	512	768	960	768	2560
Δ/η	0.76	0.74	0.85	0.86	1.23	1.4
Simulation time (ms)	20	25	30	30	30	30
Symbol	◆	◇	▽	□	●	+

TABLE 1. Numerical and physical initial parameters of the DNS. Where needed, the parameters for the non-reacting case II were re-computed with the given values for $\bar{U}_0$ and H_0.

$\chi(Z) = a\exp(-2[\mathrm{erfc}^{-1}(2Z)]^2) = 2D(Z)(\partial Z/\partial y)^2$ in the y-direction from $Z = 0$ (oxidizer) to $Z = 1$ (fuel). The mixture fraction profile starts at the edge of the channel velocity profile at $y = \pm 0.5H_0$ to provide a wider fuel slab to maintain combustion during later time steps and allow the velocity field to develop. The parameter a was chosen so that the dissipation rate at stoichiometric conditions χ_{st} is set to $\chi_{st} = 40\ \mathrm{s}^{-1}$ for the low dilution case and $\chi_{st} = 10\ \mathrm{s}^{-1}$ for the high dilution cases. This difference in the initial scalar dissipation rate is chosen because of the significantly closer proximity of the position of the initial stoichiometric mixture to the velocity profile for the high dilution cases. The temperature and species mass fractions are mapped onto the mixture fraction field from a steady state flamelet solution with a non-unity Lewis number obtained in a counterflow configuration following Pitsch & Peters (1998).

The initial profiles of the streamwise velocity component and the mixture fraction are shown in figure 3. The normalized initial velocity profiles of the reacting cases differ slightly due to the different Reynolds numbers of the turbulent channel flows used in the initialization.

In addition to the three reacting cases, a DNS of a non-reacting planar temporally evolving jet was conducted. This DNS will be referred to as non-reacting case I. The numerical set-up, domain dimensions and initial Reynolds number mirror the intermediate *Re* case. The initial velocity field is initialized using the same instantaneous velocity field of a turbulent channel flow employed in the initialization of the intermediate *Re* case. Material properties of the flow are homogeneous and obtained from the fuel composition of the reacting cases of $Y_{\mathrm{CH}_4,2} = 0.07$ and $Y_{\mathrm{N}_2,2} = 0.93$ at $T = 680$ K. A passive scalar ϕ was added, ranging from 0 to 1. The initial ϕ is that of the mixture fraction profile of the reactive case of the same Reynolds number. The Schmidt number of the passive scalar was set to $Sc_\phi = 0.77$. The ratio of the minimum Kolmogorov scale to the grid resolution is $\Delta/\eta \approx 1.1$. Finally, a non-dimensional, non-reacting DNS, from this point on referred to as non-reacting case II, will serve as another dataset to

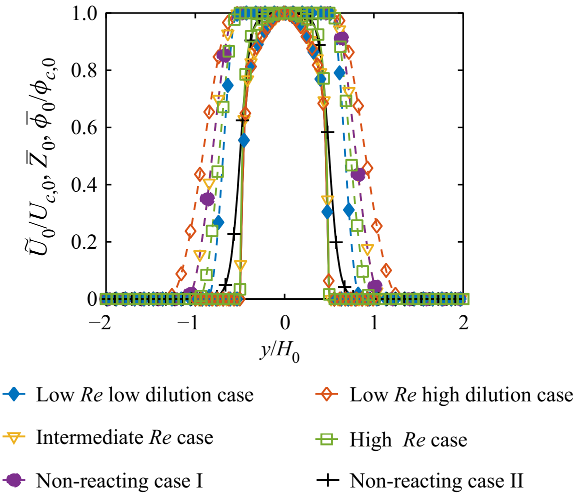

FIGURE 3. Starting profiles of the streamwise mean velocity component $\bar{U}_0$ (solid lines) and starting profiles of the mixture fraction $\bar{Z}_0$ and passive scalar ϕ_0 (dashed lines).

include a more widely used jet configuration with traditional initial solution at a higher Reynolds number (Stanley, Sarkar & Mellardo 2002; Taveira & da Silva 2013; Hunger, Gauding & Hasse 2016). This configuration possesses periodic boundary conditions in both the streamwise x and the spanwise z directions and free-slip conditions in the cross-stream direction y. The non-dimensional size of the domain is $L_x \times L_y \times L_z = 6\pi \times 12.5 \times 6\pi$. Non-dimensionalization of the transport equations is performed with the initial velocity $\bar{U}_0$, the initial jet thickness H_0 and the maximum initial scalar value $\phi_{max,0}$. The streamwisevelocity component and the passive scalar field are prescribed via a hyperbolic tangent profile. In the core region, the initial velocity is perturbed with a broadband random Gaussian velocity field derived from a one-dimensional turbulent energy spectrum to speed up the laminar–turbulent transition. The initial jet Reynolds number is set to $Re_{jet} = \bar{U}_0 H_0/\nu = 9850$. The resolution in the core region is $\Delta/\eta \approx 1.4$.

2.2. *Numerical methods*

The DNS of the reactive flows were performed with the reactive, unsteady Navier–Stokes equations in the low Mach number limit using the in-house Solver CIAO (Desjardins *et al.* 2008). The transport of species mass fractions is described using the Hirschfelder and Curtiss approximation to the diffusive fluxes together with a velocity-correction approach for mass conservation (Attili *et al.* 2016). Momentum equations are spatially discretized with a fourth-order scheme.

The disturbance pressure is obtained by solving the Poisson equation using the multi-grid solver HYPRE-AMG (Falgout, Jones & Yang 2005). Species and temperature equations are discretized with a fifth-order weighted essentially non-oscillatory (WENO) scheme (Jiang & Shu 1996). The temperature and species equations are advanced by introducing the symmetric operator split of Strang (1968). The two independent operators account for transport and reaction. The chemistry operator uses a time-implicit backward difference method (Hindmarsh *et al.* 2005). For further details about the applied numerical algorithms and code verification, the reader is referred to Desjardins *et al.* (2008). Combustion is modelled using a reduced mechanism for the oxidation of methane comprising 28 species and 102 reactions (Peters *et al.* 2002). Additionally, the formation of NO is included by means of the Zeldovich mechanism (Lavoie, Heywood & Keck 1970).

The DNS of the non-reactive flow is performed by solving the non-dimensional unsteady incompressible Navier–Stokes equations employing the in-house Solver psDNS (Göbbert *et al.* 2017). Additionally, an advection–diffusion equation is solved for a passive scalar. Spatial derivatives are calculated by the implicit sixth-order finite difference compact scheme introduced by Lele (1992). The temporal integration is performed by employing a low storage fourth-order Runge–Kutta method. The Poisson equation is solved in spectral space by adapting a Helmholtz equation (Cook, Cabot & Miller 2004).

3. Turbulent flame analysis

The overall flame evolution is shown for two different normalized time instants $t^* = 10$ and $t^* = 20$ in figure 4. The non-dimensional time t^* is defined as $t^* = (t - \Delta t_{\widetilde{\chi_{st}''^2}=0})/t_j$. The jet time is defined as $t_j = H_0/\bar{U}_0$. In addition, the duration for which the variance of the scalar dissipation rate at stoichiometric conditions is zero $\Delta t_{\widetilde{\chi_{st}''^2}=0}$ is introduced. The subtraction with $\Delta t_{\widetilde{\chi_{st}''^2}=0}$ accounts for the varying time among the cases before the turbulent central flow reaches the surface of the stoichiometric mixture fraction due to the different initial fuel slab sizes. The two time steps correspond to the time of the maximum variance of the scalar dissipation rate at stoichiometric conditions, $t^* = 10$, and the final time step in the simulations, $t^* = 20$.

The mixture fraction Z is shown in figure 4. The increase in wrinkling and folding of the flames due to turbulent advection, while present in the low dilution case, is more pronounced in the high dilution cases. High dissipation rates of the mixture fraction variance can lead to local extinction and such extinguished regions can re-ignite once the scalar dissipation rate has decreased. Although extinction and especially re-ignition do not occur instantaneously (Sripakagorn *et al.* 2004), the magnitude of the dissipation rate still provides an indication of the expected dynamics in a certain region. Regions where the scalar dissipation rate exceeds the quenching dissipation rate of the stationary flamelet solution $\chi \geq \chi_q$ are encompassed by a black contour. The regions of high χ are predominantly present in the rich regions of flow close to Z_{st}. To indicate the burning flame regions and extinguished regions of the flame, a threshold of the OH mass fraction obtained from the steady state flamelet solution $Y_{\mathrm{OH}}(x_i) = 0.01 Y_{\mathrm{OH}}(Z_{st}, \chi_q)$ is plotted as a white iso-line. As the simulations were initialized with two fully burning flames, all regions surrounding the stoichiometric mixture fraction were initially burning and consequently also contained high concentrations of OH. Therefore, at the time shown in figure 4, any stoichiometric regions with very low values of Y_{OH} are considered extinguished here and must have experienced high dissipation rates in their history. If these regions have low values of the dissipation rate at the time shown in figure 4, they might be in the process of re-igniting, which, however, is often a slow process (Sripakagorn *et al.* 2004). While all the cases display mostly intact flames, the later times show more extinguished regions in the process of re-ignition due to the aforementioned effect.

The temporal evolution of the normalized mean $\widetilde{\chi}_{st}$ at stoichiometric conditions is shown in figure 5(*a*). Qualitatively, the temporal evolutions display the same features for all cases. The shape of the temporal evolution of $\widetilde{\chi}_{st}$ is characteristic of the configuration of the planar temporally evolving jet and is observed also in other reacting and non-reacting jets (Attili *et al.* 2016; Hunger *et al.* 2016). The steep increase of $\widetilde{\chi}_{st}$ is a result of increasing gradients caused by the formation of turbulence. The scalar dissipation rate experiences

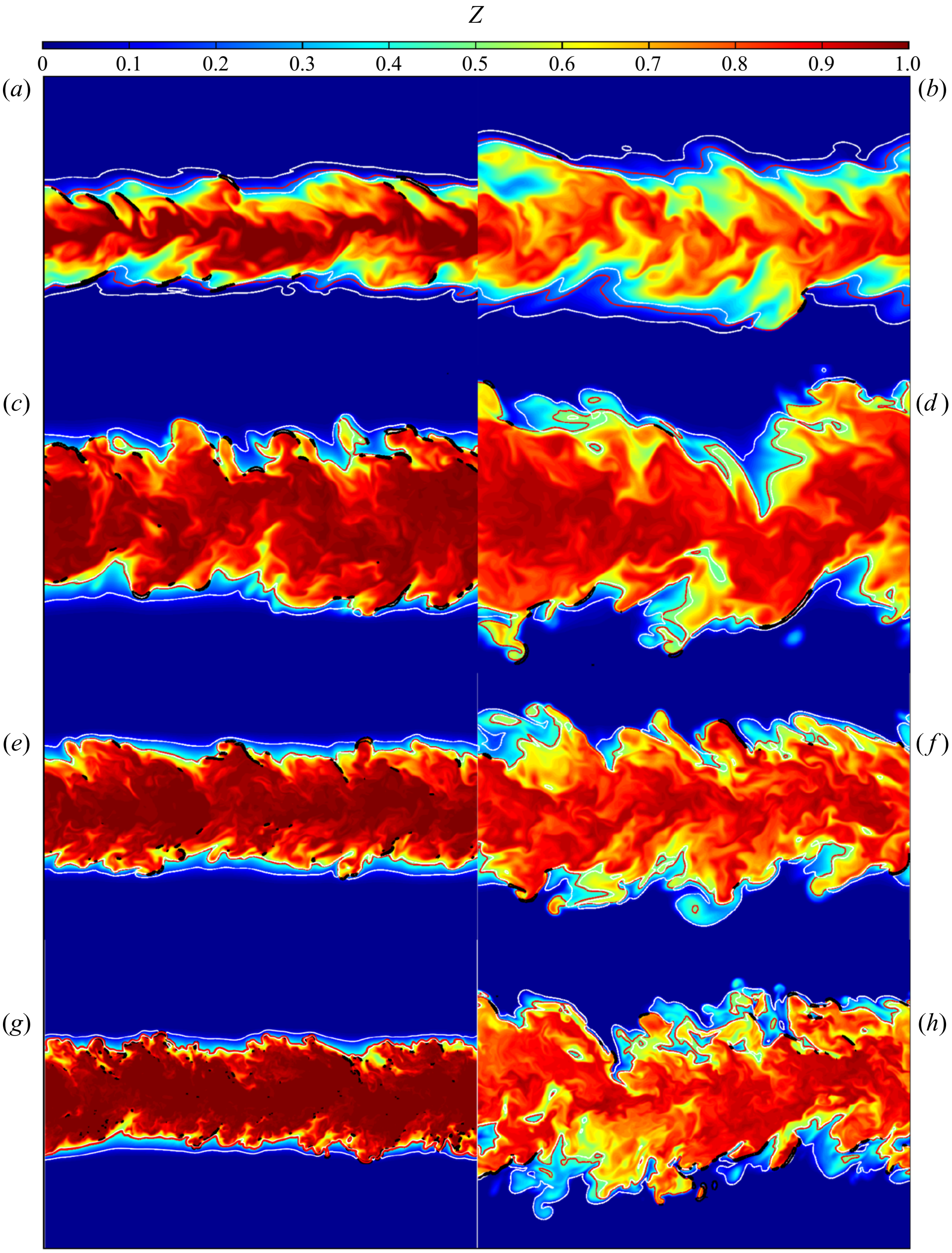

FIGURE 4. Mixture fraction Z in the x–y centre plane at time steps $t^* = 10$ (a,c,e,g) and $t^* = 20$ (b,d,f,h). From top to bottom: low *Re* low dilution case, low *Re* high dilution case, intermediate *Re* case and high *Re* case. The red colour indicates the fuel stream, blue the oxidizer. The iso-contour of the stoichiometric mixture fraction is indicated by a red line. The presence of OH is indicated by the iso-contour of $Y_{\mathrm{OH}} = 0.01 Y_{\mathrm{OH},\mathit{flamelet}}(Z_{st})$ by the white lines. The regions of quenching dissipation rates $\chi \geq \chi_q$ are indicated by black contours.

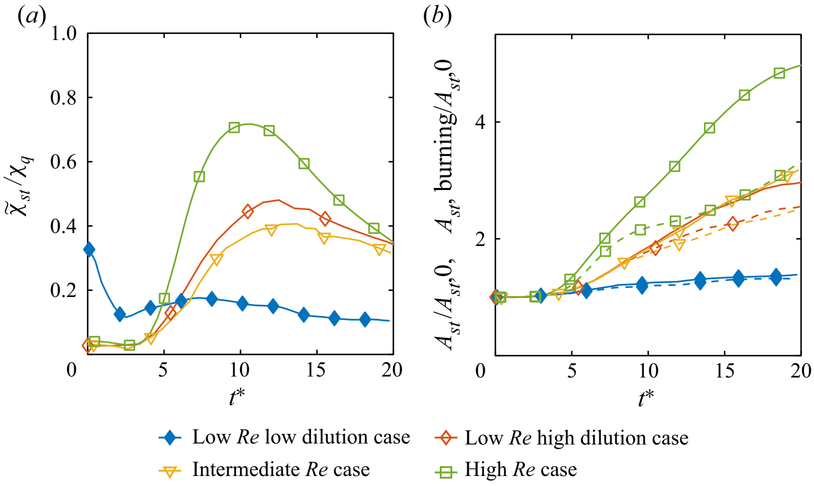

FIGURE 5. (*a*) Temporal evolution of the normalized Favre averaged scalar dissipation rate conditioned on the stoichiometric mixture fraction. (*b*) Temporal evolution of the normalized area of the iso-surface of the stoichiometric mixture fraction (solid) and burning area (dashed). Normalization is achieved with the initial stoichiometric iso-surface $A_{st,0} = 2L_xL_z$. Burning regions of the stoichiometric iso-surface are identified by thresholding the local OH mass fraction $Y_{\mathrm{OH},burning} = Y_{\mathrm{OH}}(Z = Z_{st}) \geq 0.1Y_{\mathrm{OH},flamelet}(Z_{st}, \chi_q)$.

a peak and then enters an equilibrium state with the other turbulent fields, indicated by the exponential decay. Here, gradients decrease again as a result of the increasing length scales of the system.

The temporal development of the total surface area of the stoichiometric iso-surface A_{st} is shown in figure 5(*b*). A_{st} is normalized with the initial stoichimetric iso-surface area $A_{st,0} = 2L_xL_z$. The significantly bigger difference in stoichiometric iso-surface growth between the low dilution case and high dilution cases is indicative of a higher influence of the stoichiometry than the Reynolds number in these simulations. The low Damköhler number causes local extinction, as already observed in figure 4. The burning part of the flame surface area $A_{st,burning}$ is calculated from regions with at least 10 % of the mass fraction of OH of the stationary flamelet solution at χ just below quenching conditions. The influence of localized extinction manifests itself in the departure of $A_{st,burning}$ from A_{st} after $t^* \approx 3$, which results in a final ratio of the burning area to the extinct area of the stoichiometric iso-surface of 0.95, 0.87, 0.80 and 0.75 for the low dilution low *Re* case, the high dilution low *Re*, intermediate *Re* case and high *Re* case, respectively. The overall level of extinction is in good agreement with the magnitude of χ_{st} in figure 5(*a*). The trends observed in the temporal evolution of $\widetilde{\chi}_{st}$ and A_{st} are qualitatively consistent with the observations of the extinction behaviour of turbulent non-premixed flames of Lignell, Chen & Schmutz (2011).

4. Dissipation element analysis

In the context of non-premixed flames, the mixture fraction Z is the scalar field of choice for a DE analysis, as it provides the most practical and meaningful scales for the investigation of turbulence/chemistry interaction. An exemplary interaction between a DE and the stoichiometric iso-surface, which is wrinkled by the turbulent velocity field, in the

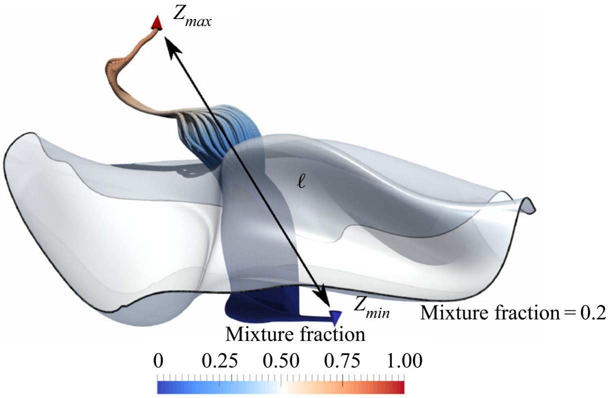

FIGURE 6. DE in interaction with the flame front in the low *Re* low dilution case. The blue and red cone indicate the maximum and minimum, respectively. The DE is represented by the gradient trajectories used in its detection. Local values of the mixture fraction are indicated by the colour of the gradient trajectories. The grey contour is the iso-surface of the stoichiometric mixture fraction $Z_{st} = 0.2$.

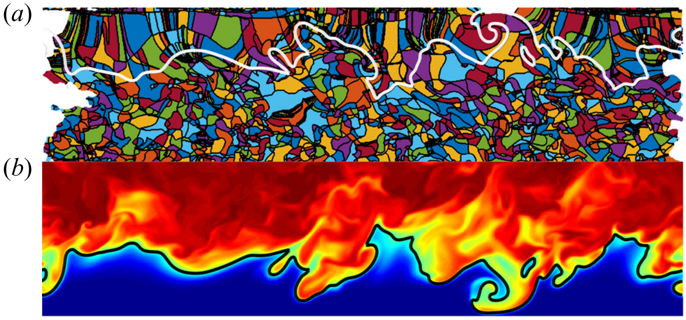

FIGURE 7. (*a*) DE analysis of the mixture fraction field of the intermediate *Re* case. Individual DEs are encompassed in a black contour. (*b*) Mirrored mixture fraction Z field on which the DE analysis was performed. Blue colour indicates the oxidizer with $Z = 0$ and red the fuel $Z = 1$.

low *Re* low dilution case is shown in figure 6. This helps to illustrate the non-trivial shape of DEs in three-dimensional space and, consequently, the complicated local structure of non-premixed combustion in the highly turbulent cases.

An entire field of DEs extracted from the intermediate *Re* case is shown in the top part of figure 7. The background field in this figure is that of the mixture fraction Z in the x–z centre plane of the turbulent jet, which is shown mirrored on the bottom part of the figure. The figure shows that dissipation elements are space-filling objects which subdivide the entire turbulent scalar field into smaller sub-units. As we follow the flame front indicated by the iso-line of the stoichiometric mixture fraction, we observe that DEs of various sizes and shapes are intersected by the flame. In addition, it can be seen that the size of the DEs increases as the core region of the jet is departed and the flame front is approached.

This observed increase in size has two reasons. Firstly, the increased diffusivity caused by the heat release as well as a mean relative velocity in the cross-stream direction cause the DE to increase in size. Secondly, the intersection area depicted here depends on the DE orientation with regard to the shown cut plane. DEs tend to be elongated tube-like structures, as seen in figure 6. Therefore, DEs oriented parallel to the x–y plane will appear significantly larger than DEs aligned with the spanwise direction. In the core of the jet, there is little to no preferential orientation of the DEs as the mixture fraction field is close to an isotropic state. However, crossing the reacting regions there are two reasons for a preferential orientation of the DEs. Due to the initialization and configuration of the cases with $Z = 1$ in the core and $Z = 0$ in the outer cross-stream position, it is more probable that the maxima are located closer to the core than the minima, which results in a natural alignment with the cross-stream direction. Additionally, the density differences cause a positive relative velocity between the extremal points spanning Z_{st}. On average, this relative velocity is the cross-stream component which further induces an orientation on the DEs in that direction.

In order to estimate the influence of small-scale turbulence in combustion, the local reaction layer thickness is typically compared to a turbulent length scale like the Kolmogorov scale η. However, in non-premixed combustion, a comparison of the reaction layer thickness with turbulent length scales in physical space does not make much sense, because the width of the layer changes locally with the mixture fraction gradient. Since the transformation in mixture fraction space makes the flame structure more general, a meaningful comparison of scales, between the scalar difference ΔZ, provided locally by the individual DEs, with the reaction layer thickness δZ_r is proposed. In this context, the DE parameter ΔZ can be interpreted as the length in Z-space in which a flamelet-like solution can exist before terminating at its respective extremal points due to the influence of turbulence. Since the gradient trajectories used to identify individual DEs are identical to the physical coordinates of flamelets, DEs can also be viewed as groupings of flamelet solutions. As the flame thickness in non-premixed flames varies greatly with the mixture fraction gradient, a second parameter to characterize DEs is instrumental in the analysis. Characterizing the scalar gradient, the parameter $g = \Delta Z/\ell$ will be used. Its square is expected to be related to the scalar dissipation rate χ as $\chi \sim Dg^2$, as was observed in isotropic turbulence by Wang & Peters (2008).

4.1. *Marginal dissipation element parameter statistics*

One of the characteristic properties of DE parameters in non-reacting flows is the invariance of the probability density functions (PDFs) of the DE length ℓ towards changes in Reynolds numbers and underlying scalar (Wang & Peters 2008; Gampert *et al.* 2013*a*). When normalized by the mean DE separation length ℓ_m, the PDFs of $\ell^* = \ell/\ell_m$ show a characteristic shape and almost perfect agreement for the entire range of investigated Reynolds numbers. Figure 8 shows the PDFs of the normalized DE parameters for the four reacting cases and the two non-reacting jets. The PDFs were obtained from the final time steps in the respective simulations and weighted with the individual DE volumes. DEs whose minima are situated outside the TNTI, as obtained by the method of Bisset, Hunt & Rogers (2002), were omitted from the statistics to rule out the inclusion of false extremal points in the laminar regions of the flows. In this fashion, 69.5 %, 85.5 %, 87.7 % and 92.1 % of the iso-surface of the stoichiometric mixture fraction is retained in the following statistics for the low *Re* low dilution case, low *Re* high dilution case, intermediate *Re* case and high *Re* case, respectively. The decreasing number of excluded DE with increasing Reynolds number is a strong indicator of the additional applicability of the method to flames with higher turbulence intensities.

In figures 8(*a*) and 8(*b*), the normalized DE length for all investigated cases is shown. The characteristic shape of the PDFs observed in the non-reactive cases is retained in the reacting simulations (Wang 2009; Gampert *et al.* 2011). After an initial

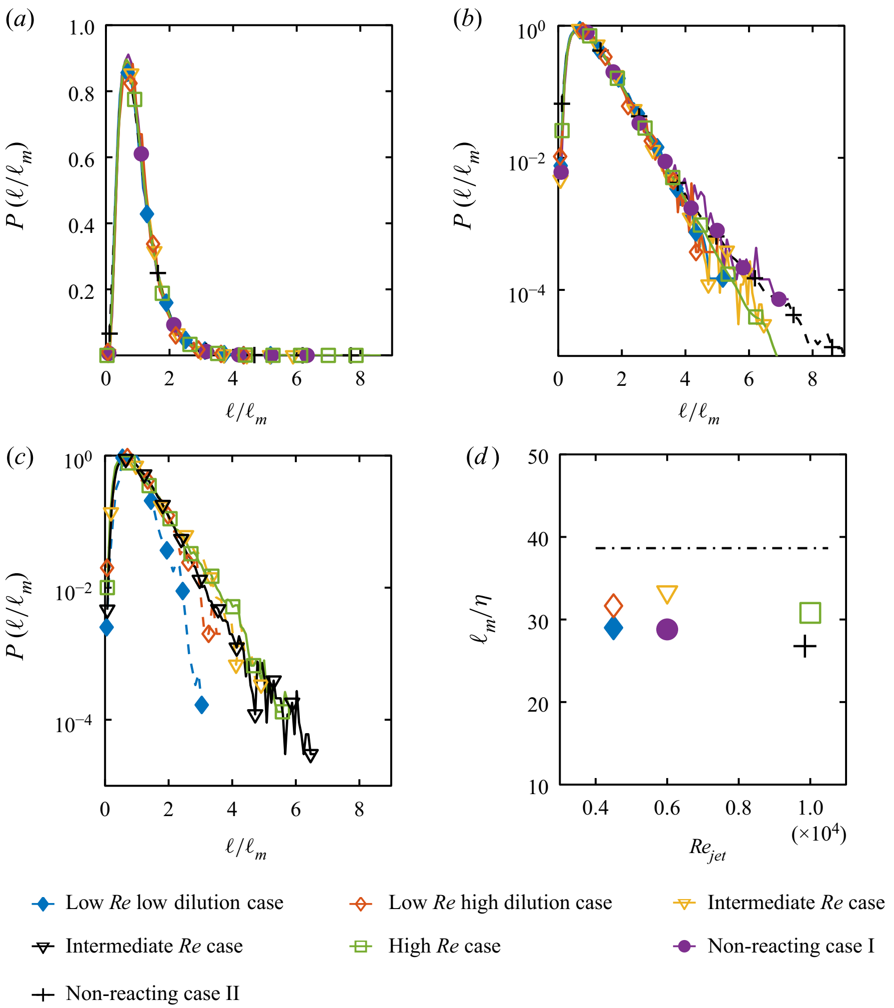

FIGURE 8. Comparison of PDFs of the normalized DE length ℓ/ℓ_m (*a*) plotted in a linear scale and (*b*) logarithmic scale. (*c*) PDF of the normalized DE length conditioned on DEs crossing the stoichiometric iso-surface (with the black line obtained from (*b*), as a reference). (*d*) Ratio of the Kolmogorov micro-scale η to the mean DE length ℓ_m for the investigated cases. The dash dotted line indicates the average ratio obtained from isotropic turbulence in Wang & Peters (2006). The line is placed arbitrarily as no jet Reynolds numbers exist.

steep linear increase for the shortest elements, a maximum of the PDFs is reached at approximately $1.6\ell^*$. This linear increase was attributed to the diffusive drift of extremal points by Wang & Peters. After the maximum, a exponential decrease of the PDF for the longer elements follows, which stems from the random cutting and reconnection process of turbulent eddies (Wang & Peters 2006). A perfect agreement is observed among all cases for the short elements. The wider separation of scales due to increasing Reynolds numbers is apparent in the tails of the PDFs which reach larger values for increasing Reynolds numbers. In figure 8(*c*), the PDF of the normalized DE length is conditioned on DEs which cross the iso-surface of the stoichiometric mixture fraction. Again, the PDFs display the characteristic course observed in the PDFs of the entire flow field. The mean

DE length ℓ_m is only slightly larger (approximately 15 %) compared to the one obtained for all DEs within the TNTI. These observations are a strong indication that the geometry of the flow and its reactive nature do not fundamentally change the characteristic length scale of turbulent structures identified by the DEs.

In figure 8(*d*), the ratio of the mean DE length and the Kolmogorov micro-scale is shown for all DEs within the TNTI. The scaling of ℓ_m with η, which was already observed for other flow configurations, is also present in the reactive flows. ℓ_m/η is approximately constant for the wide range of Reynolds numbers and configurations investigated in this work and close to the ratio observed in the isotropic configurations. In particular, the average DEs length is approximately 25–35 Kolmogorov scales. The difference in ratio with regards to the isotropic turbulence might be attributed to the presence of shear in the jet configuration.

4.2. *Joint dissipation element parameter statistics*

Figure 9 shows the joint probability density functions (jPDF) of the normalized DE length ℓ^* and the normalized scalar difference $\Delta Z^* = \Delta Z/\Delta Z_m$, with the volume-averaged scalar difference ΔZ_m, of the three jet cases in the final time step of the simulations. For the non-reacting cases in figures 9(*a*) and 9(*b*), one observes a global maximum of the probability density in the lower left corner for short elements and small scalar differences. This region of the jPDF is dominated by the diffusive drift of the extremal points leading to an annihilation of small DEs. On the top left-hand side, for small ℓ and big ΔZ, the probability of ramp-cliff structures, ubiquitously present in scalar turbulence, can be observed (Antonia & Sreenivasan 1977; Holzer & Siggia 1994). These structures are linked to external and internal intermittency and manifest themselves in very steep gradients of the scalar followed by a very gradual decent. Likewise, the scalar dissipation rate χ displays extreme spatial fluctuations. The lower right part of the jPDF, for long elements and small scalar differences, shows the regime of the physical mechanism of splitting and reconnection of DEs (Wang & Peters 2006). Qualitatively, the jPDFs of the two non-reactive cases agree.

The jPDFs of the reacting cases at low Reynolds number are shown in figures 9(*c*) and 9(*d*). Clear qualitative differences are observable compared to the non-reacting case. While the diffusive drift region of the lower part of the jPDF, for values of $\Delta Z^* < 0.8$ resembles its counterpart of the non-reacting flows, the top part looks vastly different. In addition to the local maximum probability in the diffusive drift region, the global maximum for intermediate ℓ and large ΔZ is observed for the low *Re* low dilution case. This indicates the high probability of DEs which span large mixture fraction differences almost all the way from the fuel to the oxidizer side. While the DE length distributions are unaffected by the chemical reactions, the statistics of ΔZ are heavily influenced by chemical reactions and a distinct influence of the flame structure on the DE statistics can be observed. For the jPDF of the low *Re* high dilution case, the global maximum shifts again into the diffusive drift region while the cliff structures imprinted by the flame remain more pronounced than in the non-reacting cases. These cliff structures become even less pronounced as the Reynolds number is increased in the intermediate *Re* case in figure 9(*e*), where the second local maximum for large ΔZ^* disappears. Finally, the jPDF of the high *Re* case figure 9(*f*) completely resembles the jPDFs obtained from the non-reacting cases.

The (local) maximum probability density in figures 9(*c*) and 9(*d*) stems from insufficient turbulent mixing of the mixture fraction fields in these two cases. In the very beginning of the simulations, the mixture fraction fields have no turbulent fluctuations, and because of the lack of extremal points, all DEs would be infinitely long with $\ell \to \infty$.

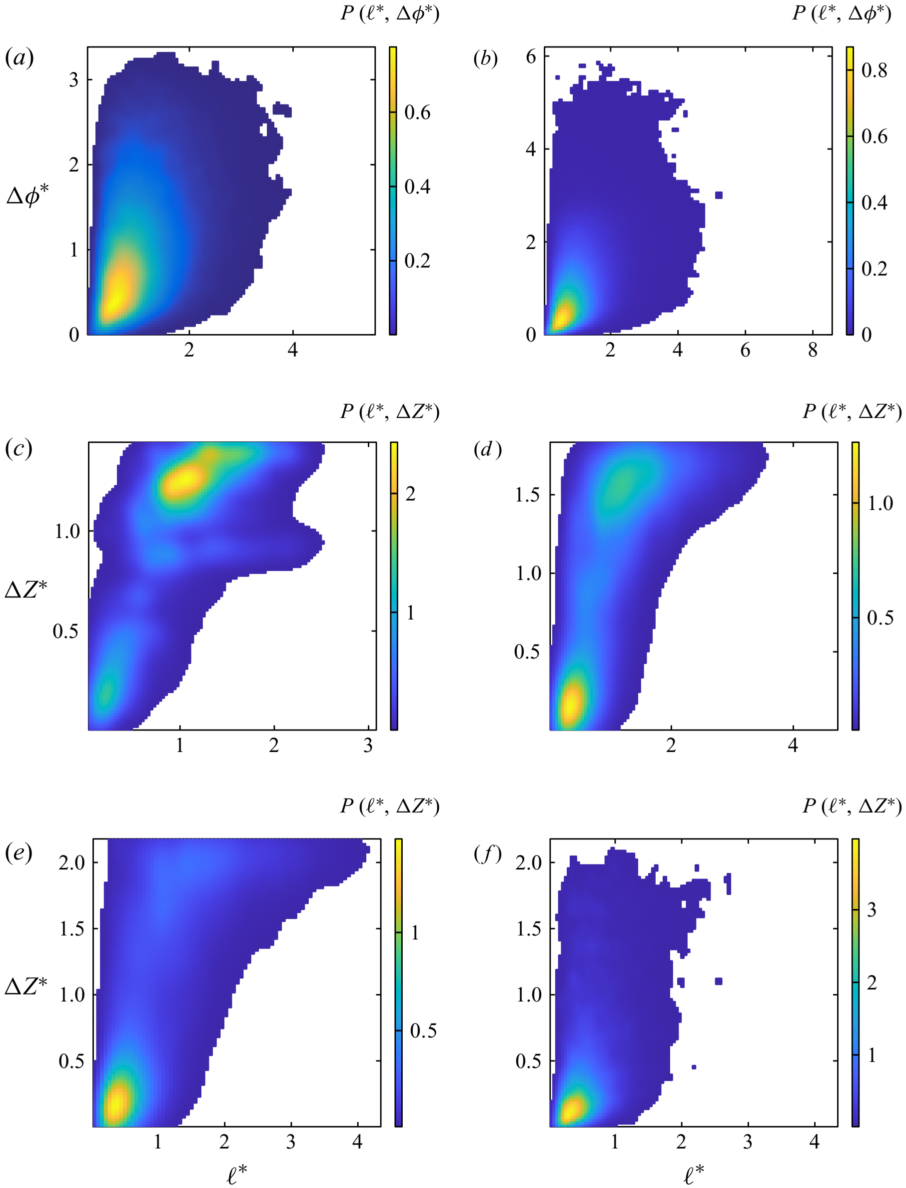

FIGURE 9. The jPDF of the normalized DE length $\ell^* = \ell/\ell_m$ and normalized scalar difference $\Delta Z^* = \Delta Z/\Delta Z_m$ in the final time step of the respective cases. (*a*) Non-reacting case I, (*b*) non-reacting case II, (*c*) low *Re* low dilution case, (*d*) low *Re* high dilution case, (*e*) intermediate *Re* case and (*f*) jPDF of the high *Re* case.

Simultaneously, all gradient trajectories would reach from $Z = 0$ to $Z = 1$. Then, the DE difference would be uniformly $\Delta Z = \Delta Z_m = 1$. As turbulent mixing is applied to the mixture fraction fields, the turbulent eddies induce extremal points which reduce both ℓ and ΔZ as time progresses. Diffusive drift will remove extremal points once elements are small enough. Therefore, the high probability of large ΔZ (in other words, close to its initial value) is a result of either not enough time for the statistics ΔZ to have fully converged at the end of the simulations, or the lack of sufficient turbulence to reach the asymptotic state observed in the non-reacting cases or in the High *Re* case. The explanation for this is twofold. The locally high diffusivity in the reacting regions smooths the scalar field and removes more extremal points in these regions. In addition, the locally low effective Reynolds number causes lower eddy turnover times. Therefore, fewer extremal points are introduced in the reacting regions.

The difference in the jPDFs between the low Reynolds number reacting and non-reacting cases could therefore be attributed to low Reynolds number effects in the reacting cases, which is amplified by heat release. Similar results with regards to trends of the effects of heat release on small-scale statistics of the velocity and mixture fraction in non-premixed flames were reported in Attili & Bisetti (2019). Additionally, this is consistent with the findings of Gauding *et al.* (2017), where a similar effect on the joint DE statistics conditioned on the flame front was observed. Likewise, the differences were linked to poor mixing in the reactive regions of the flow. This is another strong indicator that not only the marginal DE length statistics $P(\ell)$, but also the DE scalar difference statistics of passive scalars in turbulent flows share a universal form if the Reynolds number is sufficiently high, regardless of the presence of combustion and heat release. Therefore, the differences between the jPDF of the DE parameters of a passive scalar field obtained from the reacting configurations and the universal form of the jPDF might be used to judge the extent of low Reynolds number effects.

For a more quantitative way to compare the DE statistics and to relate DE parameter statistics to a more commonly used method of analysis of turbulence, the mean of the normalized DE scalar difference is conditioned on the normalized DE length $\langle \Delta Z^* | \ell^* \rangle$ and $\langle \Delta\phi^* | \ell^* \rangle$, with $\langle\rangle$ indicating the average of all grid points within the TNTI. The nth conditional moment $\langle \Delta\phi^n | \ell^* \rangle$ can be interpreted as an analogue of the conventional structure function (Wang & Peters 2006)

$$S_n(r_i) = \langle (\phi(x + r_i) - \phi(x))^n \rangle, \tag{4.1}$$

with r_i being the spatial separation between the two points. Therefore, $\langle \Delta Z^* | \ell^* \rangle$ and $\langle \Delta\phi^* | \ell^* \rangle$ resemble a first-order moment of scalar difference across a distance r_i, i.e. the first-order structure function S_1. For isotropic turbulence $\langle \Delta\phi^* | \ell^* \rangle$ was found to scale with Kolmogorov's $1/3$ power law (Wang 2009; Gampert *et al.* 2011). The mean of ΔZ^* conditioned on ℓ^* for the intermediate *Re* for all DEs within the TNTI is shown in figure 10(*a*). One observes a clear correlation between the two DE parameters for short elements with $\ell^* < 1$. The scaling exponent is significantly larger than the theoretically derived value. For larger elements, the two parameters appear to be less correlated. However, for the non-reactive case I as well as for the high *Re* in figure 10(*b*), a good collapse of the conditional means and a clear scaling of $\langle \Delta\phi^* | \ell^* \rangle$ for a wide range of ℓ^* is observed. Thus, differences in the conditioned statistics of the intermediate *Re* case can be attributed to low Reynolds number effects. The slightly larger scaling exponent displayed by the conditional means in figure 10(*b*), compared to the value usually observed in homogeneous isotropic turbulence, can be attributed to the presence of mean shear, as already observed in other non-reactive shear flows by Celani *et al.* (2005) and Attili & Bisetti (2013).

An interesting observation is that the inertial range scaling can be observed for smaller scales in the conditional mean than in regular structure functions. This has also been reported by Wang & Peters (2006), who observed the analytic inertial range scaling of $1/3$ in isotropic turbulence from scales as small as 7η. Wang and Peters showed that in the vicinity of extremal points, the scalar field is more correlated. By using the conditional

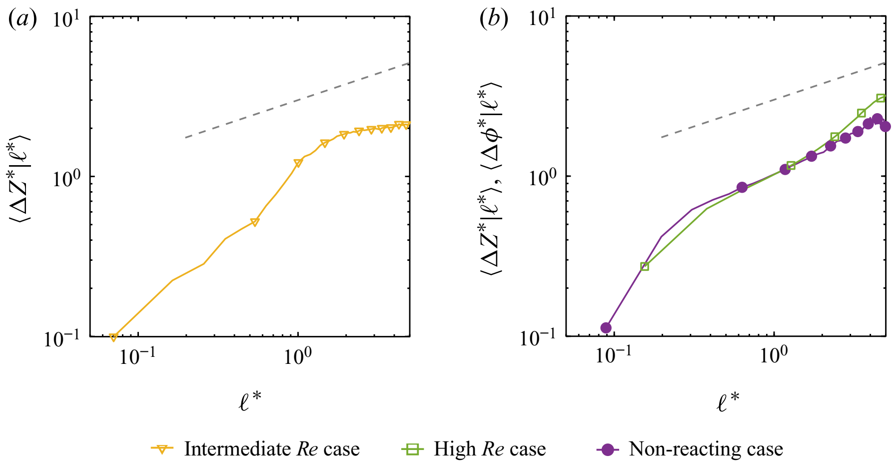

FIGURE 10. Normalized DE scalar difference conditioned on the normalized DE length $\langle \Delta Z^* | \ell^* \rangle$ and $\langle \Delta \phi^* | \ell^* \rangle$. The dashed line indicates the theoretically derived scaling.

mean $\langle \Delta Z^* | \ell^* \rangle$, i.e. conditioning the structure functions on the monotonic regions in between the extremal points, this effect is significantly reduced and an inertial range scaling is observed at smaller scales.

In the flamelet regime, the scalar dissipation rate χ serves as the parameter connecting the fields of the reactive species with the turbulent field, cf. (1.2) and (1.3). The correlation between the DE parameter and χ is therefore of high interest. Conveniently, the DE gradient $g = \Delta Z / \ell$ can be used to relate the DE parameters to the scalar dissipation rate χ. From dimensional considerations it follows that

$$\chi = 2D \left(\frac{\partial Z}{\partial x_i} \right)^2 \sim D g^2. \tag{4.2}$$

The average ratio $C_\chi = \langle \chi / (2Dg^2) \rangle$ is shown for the last time step for all investigated cases in figure 11(*a*). Regardless of configuration and Reynolds number, the average ratio displays a constant value of $C_\chi \approx 5$. This indicates for the investigated configurations that the local mixture fraction gradient, and thus, the scalar dissipation rate, can indeed be related to the gradient of the larger local flow topology, as indicated by g. Further, the ratio of the second moment to the mean DE gradient squared $\langle g^2 \rangle / g_m^2$ is shown in figure 11(*b*). No clear influence of Reynolds number is discernible and all cases display similar values for $\langle g^2 \rangle / g_m^2 \approx 1.6$. The constant value for the ratio can be explained by the universality of the normalized jPDF $P(\ell^*, \Delta Z^*)$ and the consequently universal ratio of the various moments of $g = f(\ell, \Delta Z)$. Therefore, the mean scalar dissipation rate can be related to the mean DE gradient $\langle \chi \rangle \sim \langle D \rangle g_m^2$. Consequently, this signifies that the joint DE statistics can be reconstructed, if the unconditional mean scalar dissipation rate and Kolmogorov micro-scale are known.

5. Regimes in turbulent non-premixed combustion

5.1. *Regime diagram*

One of the desirable features of DEs is their space-filling nature, enabling a unique decomposition of the entire scalar field, and therefore, the ability to locally categorize

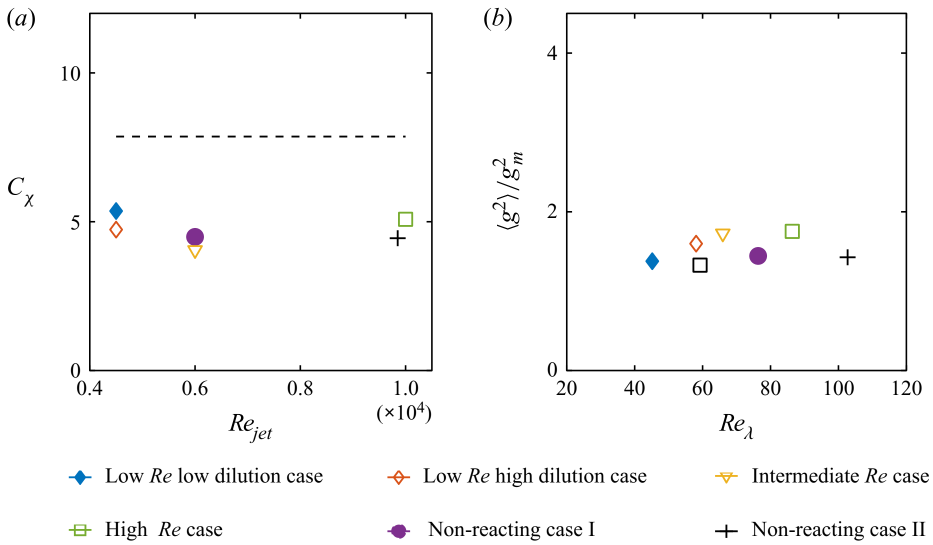

FIGURE 11. (*a*) Average ratio $C_\chi = \langle \chi / (2D \langle g^2 \rangle) \rangle$ in the final time step of the respective simulations. (*b*) Ratio of the first to the second moment of the DE scalar gradient $\langle g^2 \rangle / g_m^2$. The dashed black line and black square indicate the isotropic turbulence.

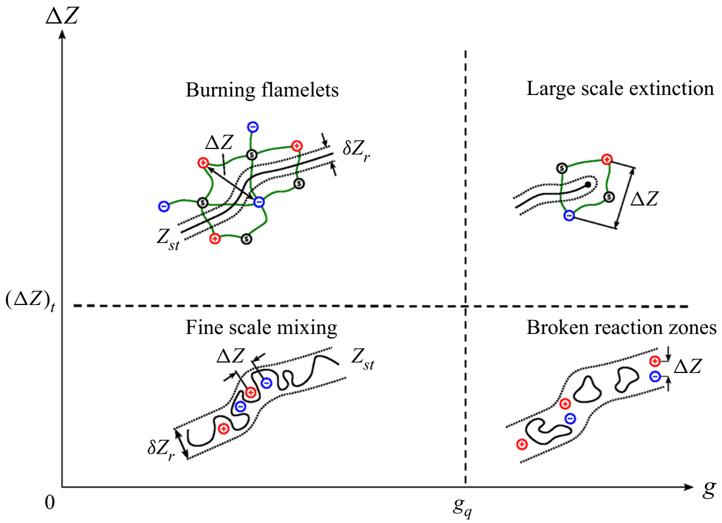

FIGURE 12. DE parameter based regime diagram for turbulent non-premixed combustion. The solid lines indicate a burning solution at Z_{st} and the dotted lines represent the thickness of the reaction zone.

the flame using the DE parameters. A categorization of combustion regimes based on DE parameters is outlined in this section. Similar to the Borghi–Peters regime diagram for turbulent premixed combustion, the turbulent scales are compared to the characteristic combustion scales. In the context of non-premixed combustion, the characteristic combustion scales are provided by the steady state flamelet solution.

The DE parameter-based regime diagram and the expected flame structure or lack thereof is depicted in figure 12.

The first DE parameter of choice is the gradient g, as it is closely related to χ, cf. figure 11(a). In the regime diagram, it represents the well-known and investigated influence of the scalar dissipation rate on the reacting scalars and is placed on the abscissa in figure 12. The first regime boundary is marked by the quenching gradient g_q, at which the heat release within the flame is insufficient to balance the energy transport caused by diffusion. In the flamelet sense, g or χ should be sufficient to characterize the reacting scalars in flows with high but finite Damköhler numbers as outlined in Peters (2010). However, to account for the interaction of chemical and turbulent scales with Damköhler numbers approaching unity, a second parameter, represented by a second coordinate in the regime diagram, is required.

Representing the effect of the different turbulent scales in the mixture fraction field, the scalar difference ΔZ fills this spot and is therefore shown on the ordinate of the regime diagram in figure 12. The scalar difference ΔZ is especially fitting, as the gradient trajectories used for the detection of DEs in the mixture fraction fields are linked to the local flamelet coordinates (Peters 2009). The turbulence-induced extremal points in the mixture fraction field represent a forced interruption of any diffusive transport, as $\nabla Z = 0$, or in the context of the flamelet equations (1.2) and (1.3), $\chi = 0$. The ΔZ of a DE including the stoichiometric iso-surface is therefore the maximum distance in Z-space in which a diffusive transport-dominated structure, such as a flamelet, can exist. Therefore, the second boundary in the regime diagram is marked by the threshold value Z-space $(\Delta Z)_t$ below which the diffusive structure of the flame is disrupted too close to the stoichiometric mixture fraction, and thus the reaction zone, to form a coherent 1-D flame structure.

The result is the definition of four regimes. In the top left, for large ΔZ and small g, the 'burning flamelet' regime is situated. Regions of the flame identified by these DE parameters should adhere to the classical steady flamelet model. The scales in the turbulent Z-field are locally large compared to those imposed by the chemistry, and the individual flamelet solutions in the DE can advance unencumbered for long distances in Z-space, from the fuel side to the oxidizer. The DE gradient stays below quenching values ensuring a burning solution.

The regime in the top right corner, called the 'large-scale extinction' regime, corresponds to large-scale extinction events, such as large rollers stemming from Kelvin–Helmholtz instabilities and the like. Here, the specified 'large scale' is the characteristic scale of the extinction-inducing event, which is large compared to the scale indicated by the local DE. Within these regions, large cliff-ramp structures with significant strain are generated. Large-scale extinct regions such as flame holes (Lu & Ghosal 2004; Pantano & Pullin 2004) correspond to this regime. The extinction in this regime corresponds to the low Damköhler type extinction caused by eddies of integral scale size. The scale of the extinction events in this regime is expected to be far larger than the individual DE volumes, and the quenching process should occur fairly instantaneously and therefore homogeneously in a single DE.

The regime in the bottom left corner is the 'fine-scale mixing' regime, for $g < g_q$ and $\Delta Z < (\Delta Z)_t$, is characterized by low gradients and small turbulent structures in the Z-field. This is indicative of very short flamelet solutions, and it is questionable if the chemical field in these regions resembles a one-dimensional solution or whether chemical reactions can be sustained. Low gradients and small scalar differences put these regions in the DE regime of 'rapid splitting and reconnection' (Wang & Peters 2008), meaning that diffusive fluxes would rapidly change direction depending on the latest pairing of the extremal points in the DE. A flame structure in the traditional sense should not exist in the regions of ‘fine-scale mixing’ if ΔZ is small enough and intense turbulent advection becomes the dominating transport mechanism. If the scalar difference is further decreased $\Delta Z < \delta Z_r$, with the thickness of the reaction zone in Z-space δZ_r, DEs may penetrate the reaction zone and exist entirely in the reaction zone. The local topology of the flame would be more akin to homogeneous reactors than flamelets.

The last remaining regime is the ‘broken reaction zone’ regime in the bottom right corner. Here one finds small scalar differences in combination with large gradients leading to small-scale extinction zones due to locally high turbulence activity. This type of extinction would correspond to a high Karlovitz-type effect, where eddies of the size of the Kolmogorov-scale transport radicals out of the inner reaction zone. Contrary to the ‘large-scale extinction’ regime, the scales of the ‘broken reaction zone’ quenching events are far smaller. Consequently, quenching would not occur homogeneously within an entire DE resulting in partially burning DEs. The resulting local topology would be characterized by small intermittent pockets of reacting and non-reacting fluid.

In a first step, to ensure that DEs represent a sensible way of decomposing the physical space into sub-units for the purpose of analysing the interaction between chemistry and turbulence, the PDF of temperature conditioned on the mixture fraction $P(T|Z)$ is compared to the conditional PDF of the DE-averaged temperature $\tilde{T}_{\mathrm{DE}}$. This average is calculated in the following way. The intersecting area of the individual DEs and the Z iso-surface is determined and the temperature in this intersecting area is then averaged. For $P(\tilde{T}_{\mathrm{DE}}|Z)$, this intersecting area additionally serves as a weight in the statistics to account for the various sizes of the DEs. The PDFs of the instantaneous temperature and the DE-averaged temperature are shown in figure 13 for the low *Re* low dilution case and intermediate *Re* case for three exemplary values of the mixture fraction. One observes a characteristic bimodal shape of the PDFs for most of the Z values, with the maximum at low temperatures corresponding to the extinct regions of the iso-surface and the maximum at high T corresponding to the burning solution. No differences between the PDFs of the temperature and the DE-averaged temperature can be observed. These results are indicative of the fact that the flow compartmentalization by means of DEs is indeed sensible, as the full PDF can be reconstructed from the DE-averaged temperature with negligible errors.

The categorization based on the proposed regime diagram in figure 12 is applied to the surface of the stoichiometric mixture fraction of the four reacting cases. The quenching gradient is estimated by using the conditional average of the DE gradient at the scalar dissipation corresponding to quenching conditions for the laminar 1-D flamelet $g_q = \langle g|\chi = \chi_q\rangle$. This results in a quenching gradient for the low *Re* low dilution case of $g_q = 110\ \mathrm{s}^{-1}$, while it is $g_q = 92\ \mathrm{m}^{-1}$, $g_q = 89\ \mathrm{m}^{-1}$ and $g_q = 90\ \mathrm{m}^{-1}$ for the low *Re* high dilution case, intermediate *Re* case and high *Re* case, respectively. The reaction thickness δZ_r in Z-space is estimated locally by fitting the inner reaction zone of the heat release profile $\omega_T(Z)$ of the steady state flamelet solution with a Gaussian profile. The reaction zone thickness is then defined as the half-width of the Gaussian. This procedure is shown for conditions close to quenching for the two investigated dilutions in figure 14(*a*). For local dissipation rates greater than the quenching dissipation rate, the reaction zone thickness at quenching conditions is chosen. The impact of the scalar dissipation rate at stoichiometric conditions on the reaction zone thickness is shown in figure 14(*b*), where an approximately 60 % wider δZ_r for the high dilution cases is observed.

The reacting scalars on the iso-surface of the stoichiometric mixture fraction are averaged conditioned on the normalized DE parameters $\Delta Z' = \Delta Z/\delta Z_r$ and $g' = g/g_q$ to achieve a comparison between the chemical and turbulent scales and check the validity

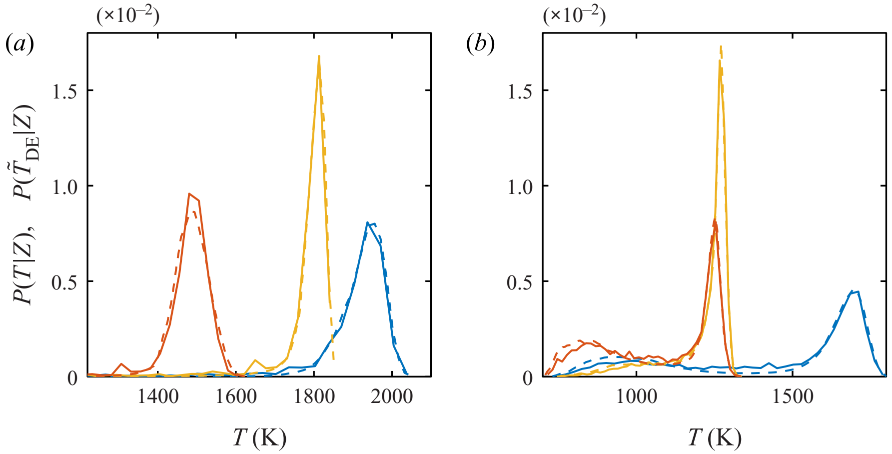

FIGURE 13. The (solid lines): PDFs of the temperature $P(T|Z)$ conditioned on three different values of the mixture fraction and (dashed lines): PDF of the temperature averaged within individual DEs $P(\tilde{T}_{\mathrm{DE}}|Z)$. Red: $Z = 0.5Z_{st}$, blue: $Z = Z_{st}$ and yellow: $Z = 1.5Z_{st}$, (*a*) low *Re* low dilution case, (*b*) intermediate *Re* case.

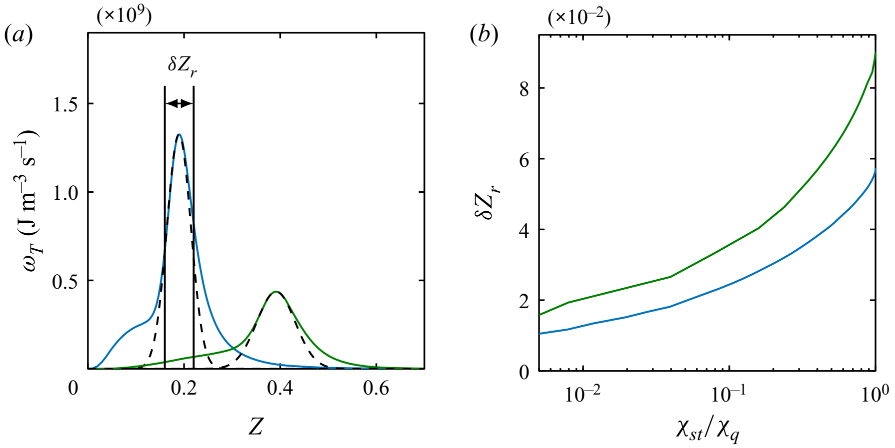

FIGURE 14. (*a*) Heat release rate ω_T for steady state flamelet solutions at quenching scalar dissipation rates (solid lines) and the inner reaction zone approximation by means of a Gaussian profile (dashed lines). Blue: low dilution corresponding to the boundary conditions in the low *Re* low dilution case, green: boundary conditions corresponding to the low *Re* high dilution case, the intermediate *Re* case and the high *Re* case. (*b*) Variation of the inner reaction zone thickness δZ_r with χ_{st}.

of the proposed regime diagram. This is shown for the temperature field for all reacting cases in figure 15 and for the OH mass fraction in figure 16. The conditional means of the reacting scalars display a good consistency with the assumptions of the previously outlined DE-based regime diagram. For all four cases, high values of the conditional means $\langle T\rangle$ and $\langle Y_{\mathrm{OH}}\rangle$ are observed for high values of $\Delta Z'$ and low values of g', which is consistent with the idea of classifying the flame as burning flamelets for these values of DE parameters. Here, the reacting scalars display the same trends with regards to

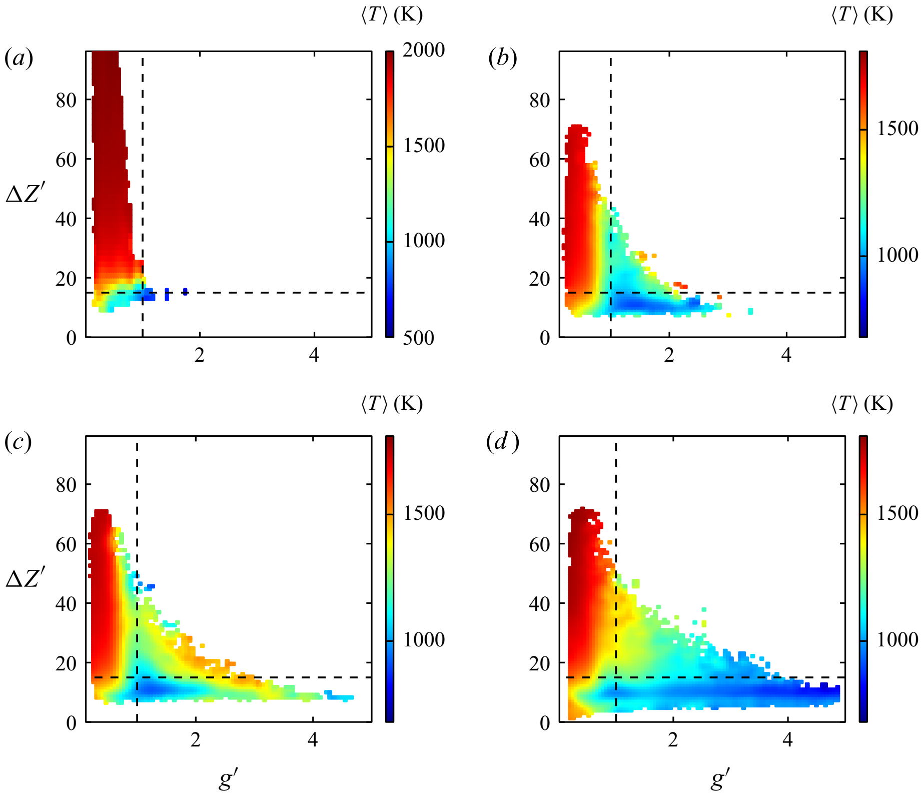

FIGURE 15. Mean temperature $\langle T\rangle$ conditioned on normalized DE parameters $\Delta Z' = \Delta Z/\delta Z_r$ and $g' = g/g_q$. Dashed lines indicate regime boundaries. (*a*) Low *Re* low dilution case, (*b*) low *Re* high dilution case, (*c*) intermediate *Re* case and (*d*) high *Re* case.

rising g' as one would expect with an increase in χ. The second regime boundary is set as $(\Delta Z)_t = 15\Delta Z'$, as the conditioned reacting scalar values decrease significantly. This value for $\Delta Z'$ is consistent across all Reynolds numbers and across the different dilutions. The reacting scalars are more susceptible to quenching caused by gradients in the mixture fraction field for $\Delta Z < (\Delta Z)_t$, as similar values of g yield significantly lower values of the mean reacting scalars.

The regime boundary at $g' = 1$ proves to be sensible as well with low values of the mean reacting scalars indicating extinction for $g' > 1$. The locally high values for $\langle T\rangle$ and $\langle Y_{\mathrm{OH}}\rangle$ in the 'large scale extinction' regime, present only in the low *Re* case and intermediate *Re* case, are not present in the high *Re* case and can be attributed to the aforementioned low Reynolds number effects which cause g and χ to be locally less correlated. The range of values of the normalized DE parameters $\Delta Z'$ and g' observed in the individual cases and the implied regime contributions to the overall combustion is consistent with the probability of observing small-scale structures in the flame and extinct regions in figure 4 and the overall levels of extinction in figure 5.

The fine-scale regimes 'fine-scale mixing' and 'broken reaction zones' are characterized by small structures in mixture fraction space and display highly turbulent behaviour. To gain a deeper understanding of the fine-scale mixing regimes, the mean temperature in the extremal points, i.e. at the minimum mixture fraction, $\langle T_{\mathrm{DE},min}\rangle$, and at the maximum

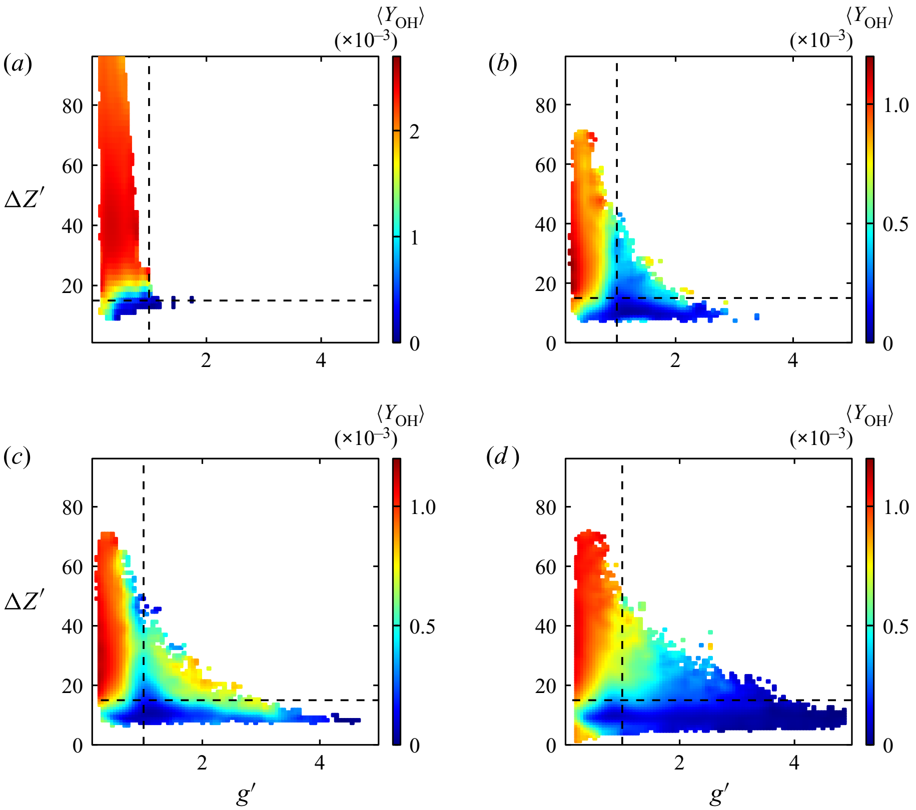

FIGURE 16. Mean OH mass fraction $\langle Y_{OH} \rangle$ conditioned on normalized DE parameters $\Delta Z'$ and g'. Dashed lines indicate regime boundaries. (*a*) Low *Re* low dilution case, (*b*) low *Re* high dilution case, (*c*) intermediate *Re* case and (*d*) high *Re* case.

mixture fraction, $\langle T_{DE,max} \rangle$, of the DEs crossing the iso-surface is conditioned on the normalized DE parameters as shown in figure 17. High values for the mean temperature in the extremal points can be observed in a triangular region for $\Delta Z' < 10$ and $g' < 1$. The values of the mean reacting scalars are comparable to those obtained at the stoichiometric iso-surface, as observed for the small $\Delta Z'$ and g' in figures 15 and 16. The presence of extremal points of the mixture fraction field within the reaction zone further validates the idea of a 'fine-scale mixing' regime. The DEs in this regime resemble fully reacting sub-regions of the flame from the minimum to maximum.

Due to the small g' in this triangular region, the ℓ of the DE occupying this part of the flame ranges from $5\eta < \ell < 50\eta$. This indicates the presence of large and fully reacting structures, which are significantly wider than the reaction zones in the flamelet solution. The values of $10 < \Delta Z' < 15$ might be viewed as a transition range between two burning regimes.

For a final analysis of the sensibility of the DE-based regime diagram and to estimate the level of extinction in the individual regimes, the marginal PDF of the temperature at stoichiometric conditions $P(T_{st})$ is additionally conditioned on the individual combustion regimes. This is shown for two time steps for the high *Re* case in figure 18. As observed in figure 13(*b*), two peaks in the PDFs are present, one for low temperatures

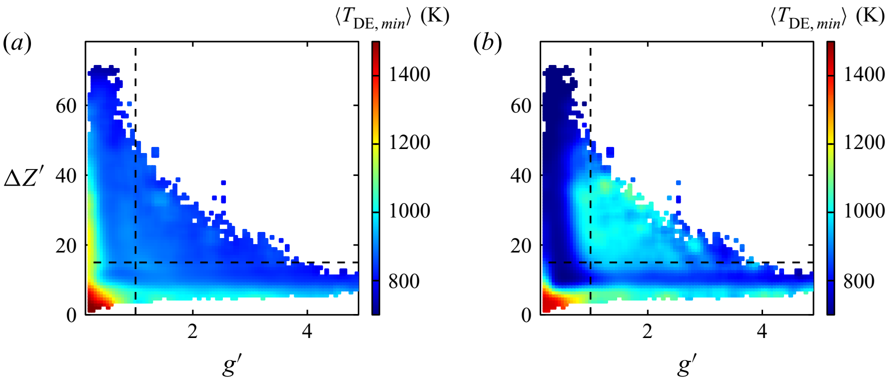

FIGURE 17. Mean temperature (*a*) in the minima $\langle T_{\mathrm{DE},min}\rangle$ and (*b*) in the maxima $\langle T_{\mathrm{DE},max}\rangle$ of DEs crossing the stoichiometric iso-surface conditioned on the normalized DE parameter g' and $\Delta Z'$ for the high *Re* case. The dashed lines indicate the regime boundaries.

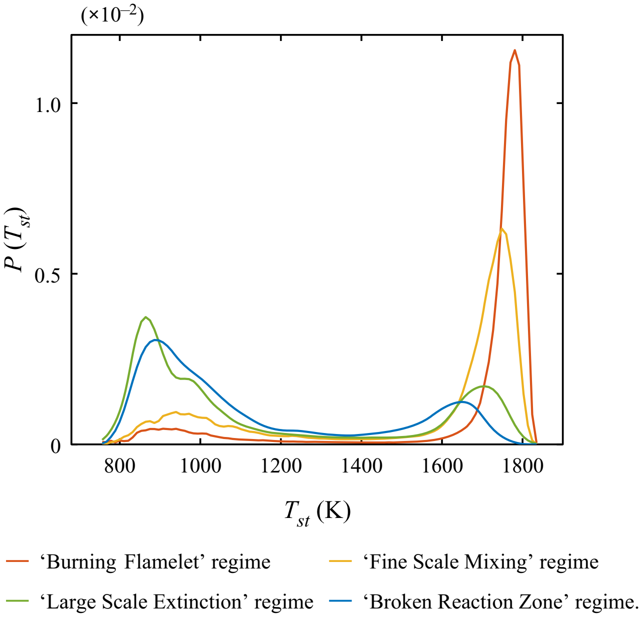

FIGURE 18. PDF of the temperature conditioned on the stoichiometric mixture fraction, and on the individual regimes in the final time step of the high *Re* case.

and one for high temperatures corresponding to burning and extinct parts of the stoichiometric iso-surface, respectively. For the extinction regimes, the global maximum of the probability density is located at low temperatures with only minor amounts in temperature ranges that can sustain combustion. The remaining low amounts of probability density of low temperature in the 'burning flamelets' regime can be explained by parts of the flow undergoing re-ignition or by locally too high values of χ for re-ignition of previously extinguished parts of the flow.

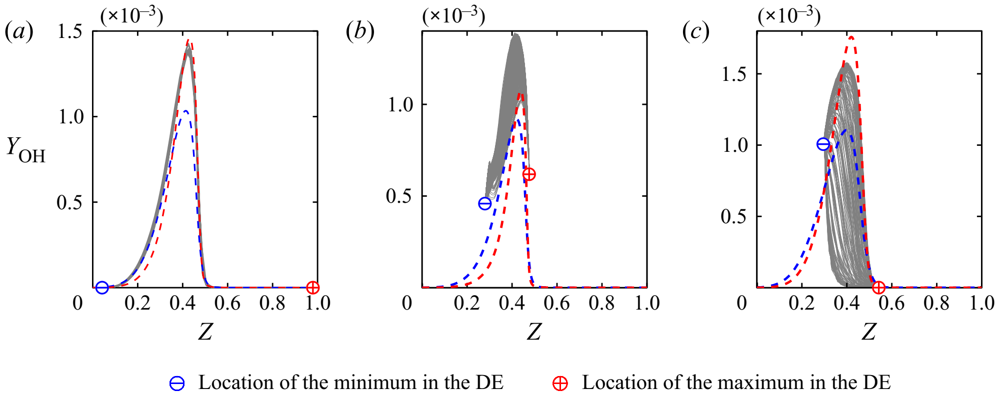

FIGURE 19. The (grey lines) mass fraction of OH radicals obtained along all gradient trajectories of a single DE. The steady state flamelet solution for the DE-averaged scalar dissipation rate at stoichiometric conditions $\widetilde{\chi_{st}}_{DE}$ is indicated by the blue dashed line and red dashed line for the non-unity Lewis number and unity Lewis number solutions, respectively. (*a*) DE obtained from the 'burning flamelet' regime, (*b*) DE from the 'fine scale mixing' regime and (*c*) DE obtained from the 'broken reaction zones' regime.

5.2. *Local flame analysis*

As the gradient trajectories in mixture fraction space are equivalent to the physical coordinates of the flamelet solution in physical space, a non-local comparison with the steady state flamelet solution in a physically meaningful framework is straightforward. For a more detailed investigation, the instantaneous mass fraction of OH obtained along all gradient trajectories used in the detection of exemplary DEs are plotted in the mixture fraction space in figure 19. This is done for three representative DEs obtained from the 'burning flamelet' regime, the 'fine-scale mixing' regime and the 'broken reaction zone' regime in the last time step of the high *Re* case. The representative DEs are obtained from burning regions of the stoichiometric iso-surface, as shown in figure 5. The DEs are of comparable volume and possess a similar intersecting area with the iso-surface of the stoichiometric mixture. Y_{OH} along the gradient trajectories is compared to the steady state flamelet solutions obtained from the steady state flamelet solution using the averaged scalar dissipation rate at the intersecting area of the DE and the stoichiometric mixture fraction iso-surface $\widetilde{\chi_{st}}_{DE}$.

For the DE obtained from the 'burning flamelet' regime, shown in figure 19(*a*), the mass fractions along the individual trajectories collapse perfectly with the unity *Le* flamelet solution for a wide range of Z values. The indiscernibility of Y_{OH} between the individual trajectories is very consistent with the flamelet assumption of a change of any reactive scalar exclusively in the Z-direction. However, for the DE obtained from the 'fine-scale mixing' regime in figure 19(*b*), Y_{OH} displays a wide range of values for a given value of Z, especially for mixture fractions close to stoichiometry. Large departures from both flamelet solutions can be observed with Y_{OH} obtained in the DE having consistently higher values, even in the extremal points. The rather large inhomogeneity of the reacting scalar on an iso-surface of Z within a small spatial sub-unit, such as a DE, clashes with the 1-D flamelet assumption, as additional transport of the reacting scalars is expected to take place tangentially to the mixture fraction coordinate. The mass fraction of OH obtained from the 'broken reaction zones' regime, shown in figure 19(*c*) shares this characteristic.

While the range of values is significantly larger than in the DEs of the other regimes, some trajectories display values corresponding to an extinct solution while others are fully burning, which is consistent with the assumption of a 'broken reaction zones' regime.

The effect of the inhomogeneity of reactive scalars for a specific iso-value of Z, which is observed for the exemplary DEs in the 'fine-scale mixing' regime and 'broken reaction zones' regime, can be statistically measured by the coefficient of variation of a reactive scalar in a DE

$$c_{v,\alpha}(Z) = \frac{\sqrt{\widetilde{\psi''^2}_{\alpha,\mathrm{DE}}(Z)}}{\tilde{\psi}_{\alpha,\mathrm{DE}}(Z)}. \tag{5.1}$$

The mean coefficient of variation of OH at stoichiometry, conditioned on the normalized DE parameters $\langle c_{v,\mathrm{OH}}(Z_{st})|g', \Delta Z'\rangle$, is shown for the low *Re* high dilution case and the intermediate *Re* case in figures 20(*a*) and 20(*b*). The coefficient of variation is low in the 'burning flamelet' regime for both cases and is also relatively low for the 'large scale extinction' regime. As partly quenched DEs would display high values of the coefficient of variation, the low values support the notion of larger extinction events where regions spanning the entire cross-section of the DE are quenched simultaneously. High values for the coefficient of variation are observed in both the 'fine-scale mixing' regime and the 'broken reaction zones' regime. This indicates that the previously observed characteristics for the three exemplary DEs in figures 19(*a*)–19(*c*) are representative of the entire flame.

The PDF of the coefficient of variation of the temperature $P(c_{v,T}(Z_{st}))$ conditioned on the individual regimes and the burning regions of the high *Re* case is shown in figure 20(*c*). It shows that previously observed behaviour of the coefficient of variation with regard to the regimes extends to the temperature field. The difference in $c_{v,T}$ between the large-scale and the fine-scale regimes is approximately one order of magnitude. While comparable to the 'large scale extinction' regime, the 'burning flamelet' regime displays the lowest $c_{v,T}$. In summary, independent of the value of g, the reacting scalar fields display high local homogeneity in the 'burning flamelet' regime and 'large-scale extinction' regime, while the 'fine-scale mixing' regime and the 'broken reaction zones' regime are characterized by turbulence-induced inhomogeneity.

5.3. *Temporal evolution of the combustion regimes*

Finally, the temporal evolution of the individual regime's contribution to the overall combustion process is investigated. Besides offering ΔZ as a value to quantify 'large-scale' or 'fine-scale' interaction, the approach of using DE parameters for a classification of the combustion regimes offers a significant additional advantage over traditional statistical methods. Instead of comparing one single characteristic turbulence scale, which is defined for the entire domain (like the Kolmogorov micro-scale η in the Karlovitz number or the eddy turnover time τ in the Damköhler number) to the characteristic flame scale, a local comparison using DE parameters is possible. Every material point on the stoichiometric iso-surface can be characterized by the two DE parameters. Therefore, all of these material points can be classified individually by the DE-based regime diagram. The large range of turbulent structures simultaneously present in the various cases consequently leads to a certain degree of coexistence of combustion regimes in the conditions investigated in this work. The substantial advantage of using a local estimate for the turbulence scales allows for the quantification of the local conditions. For the coexistence of burning and extinct regimes, this was always implicitly assumed by

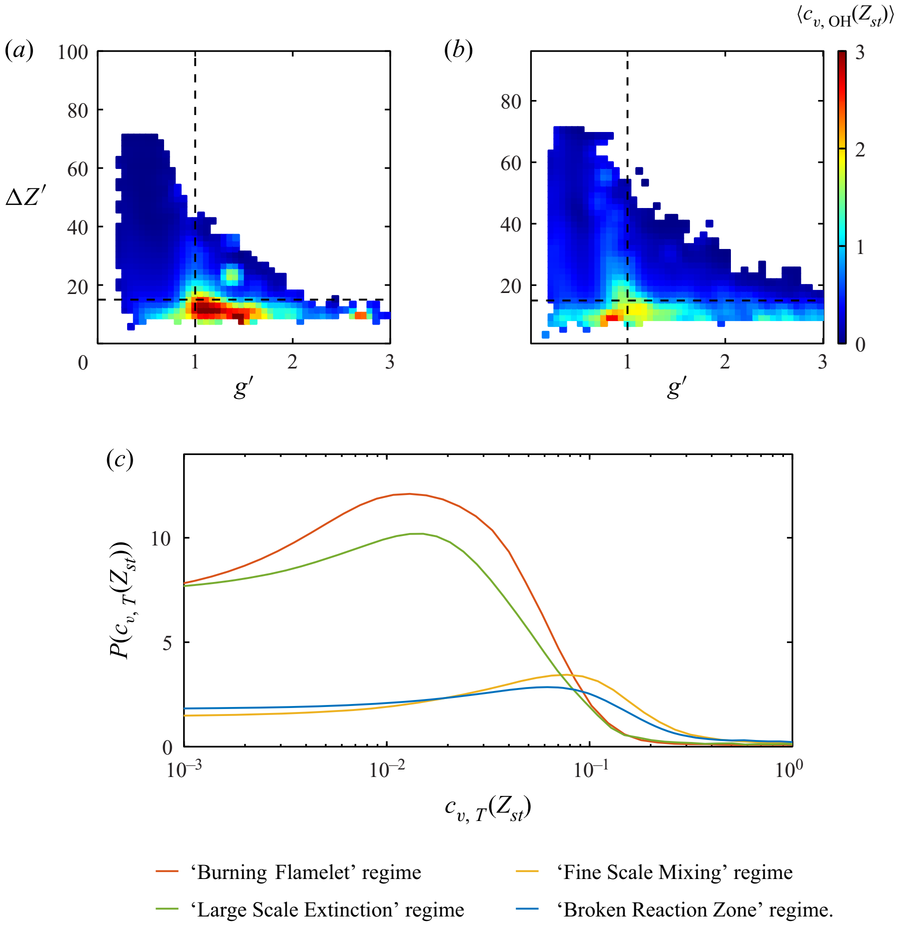

FIGURE 20. Mean DE coefficient of variation of the OH mass fraction $\langle c_{v,\mathrm{OH}}(Z_{st})\rangle$ conditioned on the normalized DE parameters g' and $\Delta Z'$ at the final time step. (*a*) Low *Re* high dilution case; (*b*) intermediate *Re* case; (*c*) PDF of the DE coefficient of variation $P(c_{v,\mathrm{OH}}(Z_{st}))$ conditioned on the individual regimes in the burning regions of the stoichiometric iso-surface for the high *Re* case.

the simultaneous presence of flame holes and edge flames in flows for which the average scalar dissipation rate remained well below quenching values (Lignell *et al.* 2011; Attili *et al.* 2015).

To achieve the local quantification of the combustion regimes, the burning area of the stoichiometric iso-surface attributed to the individual regimes in the burning regions of the flow $A_{i,st,burn}(t^*)$ is shown for all four reacting cases in figure 21(*a*). As the overall burning area increases significantly over time, normalization is achieved with the overall burning area $A_{st,burn}(t^*)$, which is identical to the one shown in figure 5(*b*).

As expected, the combustion is classified as the 'burning flamelet' regime in the early time steps of all four cases. Later, the burning regions are almost completely classified as either 'burning flamelet' regime or 'fine-scale mixing' regime. The relative contribution of the 'fine-scale mixing' regime increases with the higher dilution and the higher Reynolds number. While the 'burning flamelet' regime and the 'fine scale mixing' regimes possess

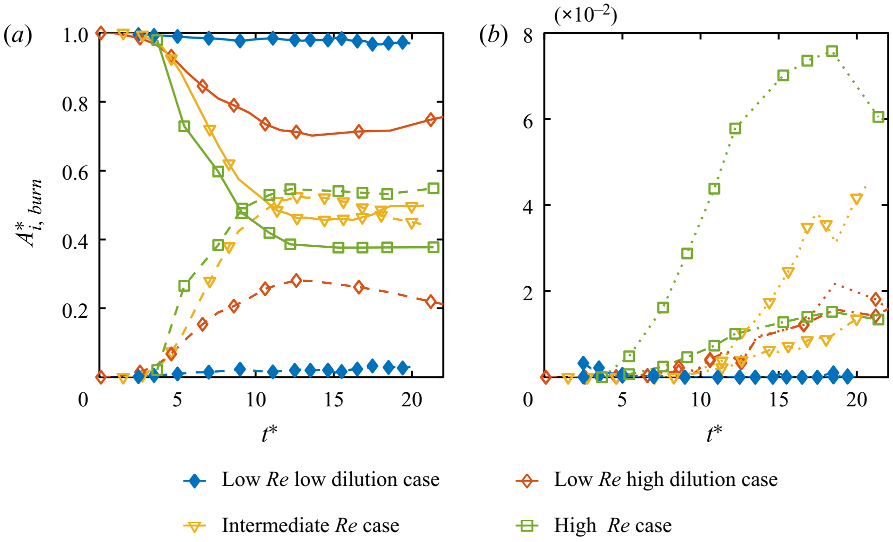

FIGURE 21. Temporal evolution of the normalized area of the stoichiometric iso-surface attributed to the individual regimes $A^*_{i,burn} = A_{i,st,burn}(t^*)/A_{st,burn}(t^*)$, conditioned on the burning regions. (*a*) Solid lines indicate the 'burning flamelet' regime and dashed lines the 'fine-scale mixing' regime. (*b*) Dash-dotted lines indicate the 'large scale extinction' regime and dotted lines the 'broken reaction zones' regime.

roughly the same area in the last time step of the intermediate *Re* case, the 'fine scale mixing' regime is the dominant regime in the final time step of the high *Re* case.

The temporal evolution of the normalized area of the stoichiometric iso-surface in the burning regions attributed to the 'large-scale extinction' regime and the 'broken reaction zones' regime is shown in figure 21(*b*). Consistent with the assumption of the regimes, the areas of both the 'large-scale extinction' regime and the 'broken reaction zones' regime are very low in the burning regions, which is emphasized by the significantly lower range of values on the ordinate. Consequently, the overall contributions of the two regimes to the stoichiometric iso-surface in the burning regions in the final time step ranges from 0 % for the low dilution low *Re* case to only 7 % in the high *Re* case.

The burning area in the two regimes might be attributed to ongoing extinction events in these time steps and is well correlated with the point in time, as well as with the ratio of burning regions of the stoichiometric iso-surface to the overall stoichiometric iso-surface, cf. figure 5(*b*). The area of the 'large scale extinction' regime is approximately the same for all three high dilution cases, which can be attributed to the comparable value of the Damköhler numbers. However, the temporal evolution of the area of the 'broken reaction zones' shows a clear dependence on the Reynolds numbers.

6. Conclusions

The DE analysis was applied to the mixture fraction fields and passive scalar fields of six reacting and inert 3-D DNS of the temporally evolving jet configuration. The statistics of the normalized DE parameter ℓ^* showed the characteristic invariance towards changes in Reynolds numbers and was unaffected by the heat release in the reacting cases. The mean DE length ℓ_m was found to scale with the Kolmogorov micro-scale. The effect of the heat release on the DE scalar difference ΔZ was observed, with an increased probability of cliff-ramp structures in the mixture fraction field. However, the effect of the heat release on the statistics decreased with an increasing dilution of the fuel stream and with an increase in the Reynolds number. The jPDF of the two normalized DE parameters obtained from the highest Reynolds number reacting case displayed the universal form observed in the non-reacting cases. DE parameter statistics were related to structure functions and the correlation between the DE gradient g and the scalar dissipation rate χ was demonstrated. This correlation allows for the reconstruction of the DE parameter statistics from the value of the unconditional scalar dissipation rate.

Additionally, a DE parameter-based regime diagram was introduced. The DE parameters g and ΔZ were compared to flame scales with the quenching gradient g_q and the reaction zone thickness δZ_r for a local classification of the flame front into four regimes. The regime assumptions were tested employing the correlation between DE parameters and reacting scalars on a non-dimensional basis. The soundness of the regime diagram was shown for all four reacting cases. Below the regime threshold value of $\Delta Z \leq (\Delta Z)_t = 15\delta Z_r$ the model assumptions of a 1-D flamelet cease to be valid as the reacting scalars display gradients in the tangential direction to the flamelet coordinates in physical space. Above this threshold value, the local conditional fluctuations of the reacting scalars are small, irrespective of the value of dissipation rate. The temporal evolution of contribution of the combustion regimes to the overall combustion was consistent with both the conventional turbulent flame analysis and the qualitative appearance of the flames in the four reacting cases.

Acknowledgements

The authors gratefully acknowledge funding from of the Deutsche Forschungsgemeinschaft (DFG) Project PE 241/441. Further, the authors gratefully acknowledge the Gauss Centre for Supercomputing e.V. (www.gauss-centre.eu) for funding this project by providing computing time on the GCS Supercomputer JUWELS at Jülich Supercomputing Centre (JSC).

Declaration of interests

The authors report no conflict of interest.

REFERENCES

ANTONIA, R. A. & SREENIVASAN, K. R. 1977 Log-normality of temperature dissipation in a turbulent boundary layer. *Phys. Fluids* **20**, 1800–1804.

ATTILI, A. & BISETTI, F. 2013 Fluctuations of a passive scalar in a turbulent mixing layer. *Phys. Rev.* E **88** (3), 033013.

ATTILI, A. & BISETTI, F. 2019 Statistics of scalar dissipation and strain/vorticity/scalar gradient alignment in turbulent nonpremixed jet flames. *Flow Turbul. Combust.* **103** (3), 625–642.

ATTILI, A., BISETTI, F., MUELLER, M. & PITSCH, H. 2016 Effects of non-unity Lewis number of gas-phase species in turbulent nonpremixed sooting flames. *Combust. Flame* **166**, 192–202.

ATTILI, A., BISETTI, F., MUELLER, M. E. & PITSCH, H. 2014 Formation, growth, and transport of soot in a three-dimensional turbulent non-premixed jet flame. *Combust. Flame* **161**, 1849–1865.

ATTILI, A., BISETTI, F., MUELLER, M. E. & PITSCH, H. 2015 Damköhler number effects on soot formation and growth in turbulent nonpremixed flames. *Proc. Combust. Inst.* **35**, 1215–1223.

BILGER, R. W., POPE, S. B., BRAY, K. N. C. & DRISCOLL, J. F. 2005 Paradigms in turbulent combustion research. *Proc. Combust. Inst.* **30**, 21–42.

Bisset, D. K., Hunt, J. C. R. & Rogers, M. M. 2002 The turbulent/non-turbulent interface bounding a far wake. *J. Fluid Mech.* **451**, 383–410.

Celani, A., Cencini, M., Vergassola, M., Villermaux, E. & Vincenzi, D. 2005 Shear effects on passive scalar spectra. *J. Fluid Mech.* **523**, 99–108.

Cook, A, Cabot, W. & Miller, P. 2004 The mixing transition in Rayleigh–Taylor instability. *J. Fluid Mech.* **511**, 333–362.

Denker, D., Attili, A., Luca, S., Gauding, M., Bisetti, F. & Pitsch, H. 2019 Dissipation element analysis of premixed jet flames. *Combust. Sci. Technol.* **191**, 1–16.

Desjardins, O., Blanquart, G., Balarac, G. & Pitsch, H. 2008 High order conservative finite difference scheme for variable density low Mach number turbulent flows. *J. Comput. Phys.* **227**, 7125–7159.

Falgout, R. D., Jones, J. E. & Yang, U. M. 2005 Pursuing scalability for hypre's conceptual interfaces. *ACM Trans. Math. Softw.* **31**, 326–350.

Favier, V. & Vervisch, L. 2001 Edge flames and partially premixed combustion in diffusion flame quenching. *Combust. Flame* **125**, 788–803.

Gampert, M., Goebbert, J. H., Schaefer, P., Gauding, M., Peters, N., Aldudak, F. & Oberlack, M. 2011 Extensive strain along gradient trajectories in the turbulent kinetic energy field. *New J. Phys.* **13**, 043012.

Gampert, M., Schaefer, P., Goebbert, J. H. & Peters, N. 2013*a* Decomposition of the field of the turbulent kinetic energy into regions of compressive and extensive strain. *Phys. Scr.* **155**, 014002.

Gampert, M., Schaefer, P., Goebbert, J. H., Wang, L. & Peters, N. 2010 Testing of model equations for the mean dissipation using Kolmogorov flows. *Flow Turbul. Combust.* **85**, 225–243.

Gampert, M., Schaefer, P. & Peters, N. 2013*b* Experimental investigation of dissipation-element statistics in scalar fields in a jet flow. *J. Fluid Mech.* **724**, 337–366.

Gauding, M., Dietzsch, F., Goebbert, J. H., Thévenin, D., Abdelsamie, A. & Hasse, C 2017 Dissipation element analysis of a turbulent non-premixed jet flame. *Phys. Fluids* **29**, 085103.

Göbbert, J. H., Iliev, H., Ansorge, C. & Pitsch, H. 2017 Overlapping of communication and computation in nb3dfft for 3D fast Fourier transformations. In *High-Performance Scientific Computing* (ed. E. Di Napoli, M.-A. Hermanns, H. Iliev, A. Lintermann & A. Peyser), pp. 151–159. Springer International Publishing.

Hawkes, E. R., Sankaran, R., Sutherland, J. C. & Chen, J. H. 2007 Scalar mixing in direct numerical simulations of temporally evolving plane jet flames with skeletal CO/H_2 kinetics. *Proc. Combust. Inst.* **31**, 1633–1640.

Hindmarsh, A. C., Brown, P. N., Grant, K. E., Lee, S. L., Serban, R., Shumaker, D. E. & Woodward, C. S. 2005 SUNDIALS: suite of nonlinear and differential/algebraic equation solvers. *ACM Trans. Math. Softw.* **31** (3), 363–396.

Holzer, M. & Siggia, E. D. 1994 Turbulent mixing of a passive scalar. *Phys. Fluids* **6**, 1820–1837.

Hunger, F., Gauding, M. & Hasse, C 2016 On the impact of the turbulent/non-turbulent interface on differential diffusion in a turbulent jet flow. *J. Fluid Mech.* **802**, R5.

Jiang, G. S. & Shu, C. W 1996 Efficient implementation of weighted ENO schemes. *J. Comput. Phys.* **126**, 202–228.

Lavoie, G. A., Heywood, J. B. & Keck, J. C. 1970 Experimental and theoretical study of nitric oxide formation in internal combustion engines. *Combust. Sci. Technol.* **1**.

Lele, S. K. 1992 Compact finite difference schemes with spectral-like resolution. *Phys. Fluids* **103**, 16–42.

Lignell, D. O., Chen, J. H. & Schmutz, H. A. 2011 Effects of Damköhler number on flame extinction and reignition in turbulent non-premixed flames using DNS. *Combust. Flame* **158** (5), 949–963.

Lu, Z. & Ghosal, S. 2004 Flame holes and flame disks on the surface of a diffusion flame. *J. Fluid Mech.* **513**, 287–307.

Luca, S., Attili, A., Lo Schiavo, E., Creta, F. & Bisetti, F. 2019 On the statistics of flame stretch in turbulent premixed jet flames in the thin reaction zone regime at varying Reynolds number. *Proc. Combust. Inst.* **37** (2), 2451–2459.

Ol'shanskii, M. A. & Staroverov, V. M. 2000 On simulation of outflow boundary conditions in finite difference calculations for incompressible fluid. *Intl J. Numer. Meth. Fluids* **33**, 499–534.

PANTANO, C. & PULLIN, D. I. 2004 A statistical description of turbulent diffusion flame holes. *Combust. Flame* **137**, 295–305.

PETERS, N. 1984 Laminar diffusion flamelet models in non-premixed turbulent combustion. *Prog. Energy Combust. Sci.* **10**, 319–339.

PETERS, N. 2009 Multiscale combustion and turbulence. *Proc. Combust. Inst.* **32**, 1–25.

PETERS, N. 2010 *Combustion Theory*. CEFRC Summer School Princeton.

PETERS, N. 2012 Turbulence statistics along gradient trajectories. *Z. Angew. Math. Mech.* **92**, 4–7.

PETERS, N., PACZKO, G., SEISER, R. & SESHADRI, K. 2002 Temperature cross-over and non-thermal runaway at two-slage ignition at n-heplane. *Combust. Flame* **128**, 38–59.

PITSCH, H. & PETERS, N. 1998 A consistent flamelet formulation for nonpremixed combustion considering differential diffusion effects. *Combust. Flame* **114**, 26–40.

POPE, S. B. 2013 Small scales, many species and the manifold challenges of turbulent combustion. *Proc. Combust. Inst.* **34**, 1–31.

SCHNORR, A., HELMRICH, D., DENKER, D., KUHLEN, T. & HENTSCHEL, B. 2020 Feature tracking by two-step optimization. *IEEE Trans. Vis. Comput. Graphics* **26** (6), 2219–2233.

SRIPAKAGORN, P., MITARAI, S., KOSALY, G. & PITSCH, H 2004 Extinction and reignition in a diffusion flame (a direct numerical simulation study). *J. Fluid Mech.* **518**, 231–259.

STANLEY, S., SARKAR, S. & MELLARDO, J. P 2002 A study of the flowfield evolution and mixing in a planar turbulent jet using direct numerical simulation. *J. Fluid Mech.* **450**, 377–407.

STRANG, G. 1968 On the construction and comparison of difference schemes. *SIAM J. Numer. Anal.* **5**, 506–517.

TAVEIRA, R. R. & DA SILVA, C. B. 2013 Kinetic energy budgets near the turbulent/nonturbulent interface in jets. *Phys. Fluids* **25**, 015114.

WANG, L. 2009 Structure function of two-point velocity difference along scalar gradient trajectories in fluid turbulence. *Phys. Rev.* E **79**, 046325.

WANG, L. & PETERS, N. 2006 The length scale distribution function of the distance between extremal points in passive scalar turbulence. *J. Fluid Mech.* **554**, 457–475.

WANG, L. & PETERS, N. 2008 The length scale distribution functions and conditional means for various fields in turbulence. *J. Fluid Mech.* **608**, 113–138.

WANG, L. & PETERS, N. 2013 A new view of flow topology and conditional statistics in turbulence. *Phil. Trans. R. Soc.* A **371**, 20120169.